



Published in final edited form as:

Cell Rep. 2021 May 11; 35(6): 109106. doi:10.1016/j.celrep.2021.109106.

## Microcircuit mechanisms for the generation of sharp-wave ripples in the basolateral amygdala: A role for chandelier interneurons

Madhusoothanan B. Perumal<sup>1</sup>, Benjamin Latimer<sup>2</sup>, Li Xu<sup>1</sup>, Peter Stratton<sup>1</sup>, Satish Nair<sup>2</sup>, Pankaj Sah<sup>1,3,4,\*</sup>

<sup>1</sup>Queensland Brain Institute, The University of Queensland, Brisbane, QLD 4072, Australia

<sup>2</sup>Electrical Engineering & Computer Science, University of Missouri, Columbia, MO 65211 USA

<sup>3</sup>Joint Center for Neuroscience and Neural Engineering and Department of Biology, Southern University of Science and Technology, Shenzhen, Guangdong Province 518055, P.R. China

<sup>4</sup>Lead contact

### SUMMARY

Synchronized activity in neural circuits, detected as oscillations in the extracellular field potential, has been associated with learning and memory. Neural circuits in the basolateral amygdala (BLA), a mid-temporal lobe structure, generate oscillations in specific frequency bands to mediate emotional memory functions. However, how BLA circuits generate oscillations in distinct frequency bands is not known. Of these, sharp-waves (SWs) are repetitive, brief transitions that contain a low-frequency (<20 Hz) envelope, often coupled with ripples (100–300 Hz), have been associated with memory consolidation. Here, we show that SWs are retained in the BLA *ex vivo* and generated by local circuits. We demonstrate that an action potential in a chandelier interneuron is sufficient to initiate SWs through local circuits. Using a physiologically constrained model, we show that microcircuits organized as chandelier-interneuron-driven modules reproduce SWs and associated cellular events, revealing a functional role for chandelier interneurons and microcircuits for SW generation.

### Graphical Abstract

This is an open access article under the CC BY-NC-ND license (<http://creativecommons.org/licenses/by-nc-nd/4.0/>).

\*Correspondence: [pankaj.sah@uq.edu.au](mailto:pankaj.sah@uq.edu.au).

#### AUTHOR CONTRIBUTIONS

P.S. and M.B.P. conceived of the experiments; M.B.P. performed experiments and analyzed electrophysiology data. L.X. made viral vectors. P. Stratton analyzed data. S.N., M.B.P., P.S., and B.L. conceived the model; S.N. and B.L. implemented the model. P.S., M.B.P., S.N., and B.L. wrote the paper.

#### DECLARATION OF INTERESTS

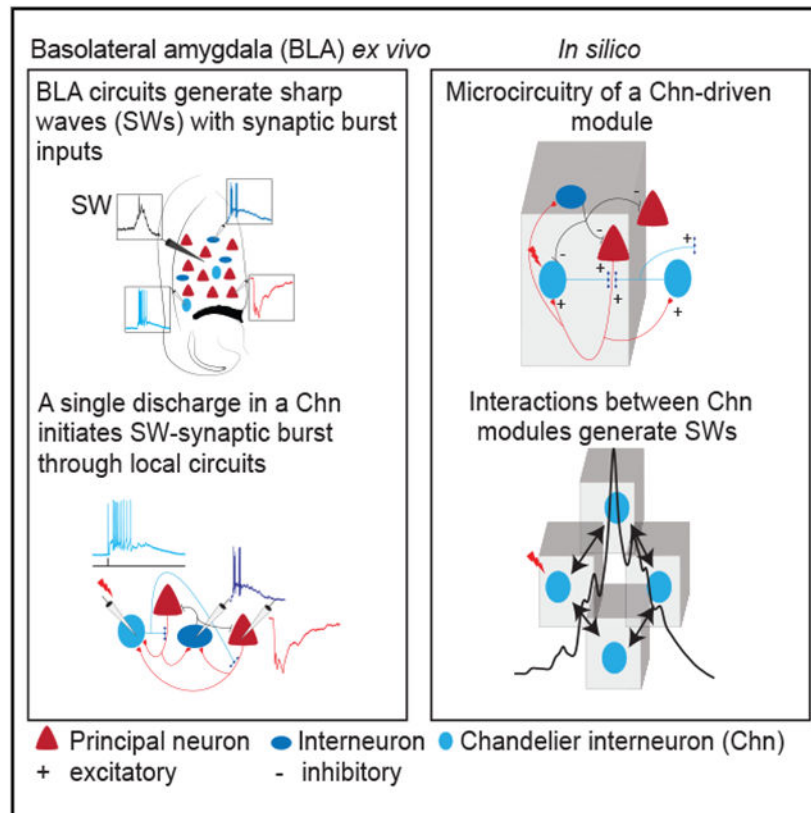
The authors declare no competing interests.

#### SUPPLEMENTAL INFORMATION

Supplemental information can be found online at <https://doi.org/10.1016/j.celrep.2021.109106>.

#### SUPPORTING CITATIONS

The following references appear in the supplemental information: Alturki et al. (2016); Carnevale and Hines (2006); Destexhe et al. (1994); Durstewitz et al. (2000); Einevoll et al. (2013); Feng et al. (2016); Galarreta and Hestrin (1997); Gold et al. (2006); Goto et al. (2010); Hummos et al. (2014); Kim et al. (2013); Li et al. (2009); Magee et al. (1998); Migliore et al. (1999); Pape et al. (1998); Parasuram et al. (2016); Power et al. (2011); Schomburg et al. (2012); Traub et al. (2003); Washburn and Moises (1992).



## In brief

Perumal et al. investigate circuits that generate network oscillations called sharp waves (SWs) in the basolateral amygdala. They show that discharge in a chandelier interneuron can initiate SW oscillations—a network activity associated with memory consolidation. They develop a network model with chandelier-interneuron-driven modular microcircuits for SW generation.

## INTRODUCTION

The ability to remember and respond to salient events is crucial for the survival of all organisms. The storage and retrieval of memories is associated with oscillatory network activity that is detected as rhythmic changes in the local field potential (LFP) (Buzsáki, 2006). Of these, SWs are brief transitions in the LFP lasting 50–100 ms that contain a low-frequency (<20 Hz) envelope, often associated with time-locked high-frequency (100–300 Hz) oscillations called ripples. SWs have been observed in many brain regions, are particularly evident during slow wave sleep, and have been associated with memory consolidation and retrieval (Axmacher et al., 2006; Buzsáki, 2006, 2015; Joo and Frank, 2018). They have been extensively studied in the hippocampus, and a number of different circuit models have been proposed to explain their generation (Buzsáki, 2015). However, how SWs are initiated and the mechanisms that generate their stereotypical time course and termination remain controversial (Buzsáki, 2015; Csicsvari et al., 2000; Ramirez-Villegas et al., 2018).

The basolateral amygdala (BLA), a part of the amygdalar complex (Sah et al., 2003), plays a key role in assigning emotional valence to sensory stimuli, particularly fear (McGaugh, 2004; O'Neill et al., 2018; Pignatelli and Beyeler., 2019). Neural circuits within the BLA generate a host of different oscillations (Bocchio et al., 2017; Haufler and Pare, 2014; Paré et al., 2002), including SWs (Ponomarenko et al., 2003) that are associated with learning, memory consolidation, and retrieval of emotionally salient events (Bocchio et al., 2017; Paré et al., 2002). The BLA is a cortical-like structure that contains glutamatergic principal neurons (PNs) that make ~80% of the total neuronal pool, with the remaining 20% comprising a diverse population of GABAergic interneurons (INs) (Polepalli et al., 2020; Sah et al., 2003; Spampanato et al., 2011). Intracellular recordings in acute *ex vivo* studies have found that neurons in the BLA show spontaneous periodic changes in membrane potential, during which PNs receive a burst of inhibitory synaptic input and INs a correlated burst of excitatory input, of which both are blocked by GABA<sub>A</sub> receptor antagonists (Chung and Moore, 2009; Popescu and Paré, 2011; Rainnie, 1999; Rainnie et al., 2006; Ryan et al., 2012), indicating a crucial role for GABAergic transmission in both events. The mechanism that generates this spontaneous activity in the BLA is not understood, but it resembles SW-associated synaptic events described in pyramidal neurons and INs in the hippocampus (English et al., 2014; Maier et al., 2003; Schlingloff et al., 2014). However, whether SWs are present in the BLA slices *ex vivo* is not known.

Chandelier INs are a specialized class of parvalbumin (PV)-expressing INs that make axo-axonic synapses on glutamatergic PNs (Howard et al., 2005). Although these cells form less than 3% of the total IN pool, single chandelier INs innervate hundreds of PNs (Howard et al., 2005; McDonald and Bette, 2001; Woodruff et al., 2010) and have been suggested to influence network activity in the BLA (Bienvenu et al., 2012). Here, we show that spontaneous SWs are present in acute brain slices of the BLA maintained *ex vivo*, showing they are generated by local circuit mechanisms. We show that a single action potential in a chandelier IN is sufficient to initiate SWs, engaging glutamatergic PNs and GABAergic INs. We describe an experimentally constrained network model of the BLA, with circuits organized as chandelier-IN-driven modules, that reproduces the synaptic activity, frequency components, and time course of SWs. This study provides a functional role for chandelier INs in driving network oscillations and a circuit mechanism for the initiation, time course, and termination of SWs.

## RESULTS

### Sharp-wave ripples in the BLA

To investigate network activity in the BLA, we obtained LFP recordings in oblique horizontal brain slices (Figure 1; Figure S1A). In this preparation, the LFP showed spontaneous transitions (Figure 1A) at a rate of ~30 events/min ( $n = 25$  slices). These events had a low-frequency (1–20 Hz) envelope with a half-width of  $40 \pm 7$  ms and were occasionally accompanied with phase locked with high-frequency (100–300 Hz) oscillations (Figures 1A and 1B). Spectral analysis of these LFP transitions confirmed enhanced power in low and ripple frequency bands (Figure 1B), similar to SWs described in the BLA *in vivo*

(Ponomarenko et al., 2003) and the hippocampus *in vivo* (Buzsáki et al., 1992) and *ex vivo* (Maier et al., 2003; reviewed in Buzsáki, 2015).

To understand the intracellular activity during SWs (SWi), simultaneous whole-cell recordings were obtained from BLA neurons. INs were distinguished from PNs (Figures S1B-S1E) by using action potential discharge properties (Mahanty and Sah, 1998) or the presence of GFP in slices prepared from transgenic mouse lines (GAD67-EGFP or PV-EGFP). These recordings revealed that in PNs, extracellular SWs were accompanied by an inhibitory postsynaptic potential (IPSP; Figure S1F; mean amplitude  $-7.5 \pm 2$  mV;  $n = 87$  cells) and occasional action potential (see below). This SW-associated IPSP reversed near the predicted  $\text{Cl}^-$  equilibrium potential ( $-60$  mV; Figure 1E; Figure S1H), showing that it was predominantly mediated by  $\text{GABA}_A$  receptors. In contrast, INs received a depolarizing input during each SW, which drove a burst of action potentials (Figures 1C, 1F, and 1G; Figure S1F, left). Paired recordings showed that synaptic input to both cell types began early during the rising phase of the SW, and excitatory drive to INs slightly preceded the inhibition in PNs (Figures 1D and 1G). Previous intracellular recordings in *ex vivo* slices in rodent (Chung and Moore, 2009; Popescu and Paré, 2011; Rainnie, 1999) and primate BLA (Ryan et al., 2012) have reported similar, time-locked spontaneous synaptic events in PNs and INs, and our results show that these events are correlated with SWs (Figures S1F, S1G, and S2).

To determine the nature of synaptic input that drives these changes in membrane potential, PNs ( $n = 37$ ) and INs ( $n = 27$ ) were voltage clamped (Figure 1H; Figure S1F, right). These recordings revealed that during SWs, PNs received a summing burst of inhibitory post-synaptic currents (IPSCs; peak amplitude,  $200 \pm 86$  pA; Figure 1H), and INs received a similar burst of excitatory postsynaptic currents (SW-EPSCs; peak amplitude,  $878 \pm 582$  pA; Figure 1H; Figure S1E, right). These SW-associated synaptic bursts had a stereotypical configuration, with 4–6 synaptic currents at  $\sim 4$ -ms intervals that summated to a peak (Figure 1H). In each cycle, excitatory input to INs preceded the inhibitory input to PNs, but the overall temporal structure of both inputs was similar: (1) synaptic inputs summated to the peak within a similar time window ( $19 \pm 9$  ms in PNs and  $20 \pm 9$  ms in INs; Figure 1I); (2) spectral analysis shows that both have a low-frequency component at 1–20 Hz and a high-frequency component at 200–250 Hz (Figure 1J); and (3) the total burst duration was similar, being  $138 \pm 65$  ms in PNs and  $153 \pm 74$  ms in INs. Application of either a  $\text{GABA}_A$  receptor antagonist (10 mM bicuculline or 3  $\mu\text{M}$  gabazine,  $n = 15$ ) or  $\alpha$ -amino-3-hydroxy-5-methyl-4-isoxazolepropionic acid (AMPA) receptor antagonist (NBQX or CNQX; 10  $\mu\text{M}$ ;  $n = 12$ ) eliminated SWs and SWi-associated intracellular synaptic events (Figure 1K; Figure S1I). These results show that network activity within intrinsic circuits of the BLA generates SWs, during which PNs receive a temporally organized burst of  $\text{GABA}_A$ ergic input and INs receive a similar burst of glutamatergic input. The finding that glutamatergic input to INs during SWs can be blocked by  $\text{GABA}_A$  receptor antagonists suggests that this glutamatergic burst is driven by IN activity.

### Axo-axonic chandelier INs initiate sharp waves

Fast-spiking, PV-expressing INs form the major population (~40%) of INs in the BLA that can be separated into the following two distinct families: axo-somatic basket INs (~95%) that innervate the soma of PNs and axo-axonic chandelier INs (~5%) that innervate the axon initial segment (AIS) (McDonald, and Betette, 2001; Spampanato et al., 2011). Whole-cell recordings from PV-expressing INs in *ex vivo* slices have shown that in some INs, action potential discharge can evoke a time-locked, feedback excitatory synaptic input (Spampanato et al., 2016; Woodruff et al., 2006). This feedback excitatory input is disynaptic with a latency of ~4 ms and shows a dual pharmacological sensitivity to AMPA and GABA<sub>A</sub> receptor antagonists (Woodruff et al., 2006). Anatomically, PV-INs with this characteristic feedback excitation are chandelier INs (Woodruff et al., 2006; Spampanato et al., 2016; Szabadics et al., 2006). This dual pharmacological sensitivity of this feedback current is similar to the synaptic burst seen during SWs (Figure 1). We therefore investigated a role of these INs in the generation of SWs. As previously shown (Spampanato et al., 2016; Woodruff et al., 2006), these cells were identified electrophysiologically by using the presence of time-locked feedback excitatory synaptic input evoked by single action potentials (Figures 2A and 2B). From a total of 433 INs, an action potential evoked feedback excitation with a high success rate (83% ± 18% trials; Figure 2A, top) in 102 cells (15/82 cells recorded using PV-EGFP slices). In 19 of these INs, a single action potential could also evoke a multi-synaptic feedback burst that drove these cells to the threshold (Figure 2A, bottom). Under voltage clamp, a brief voltage step (0.5 ms) to 0 mV (Holding potential, V<sub>h</sub> = -70 mV) in these neurons evoked an unclamped discharge current, mimicking an action potential, and initiated a burst of feedback EPSCs (Figure 2B) in 40% ± 26% of trials. This evoked feedback burst had a stereotypical waveform with summing EPSCs time locked at ~4-ms intervals and a consistent intrinsic frequency of ~250 Hz (Figures 2B and 2E; Figures S3A and S3B).

The evoked feedback burst also had a dual pharmacological sensitivity, being blocked by either AMPA receptor antagonists (10 μM CNQX/NBQX ; n = 6) or GABA<sub>A</sub> receptor antagonists (10 μM bicuculline, 100 μM picrotoxin, or 3 μM gabazine; n = 15; Figure 2C; Figure S3C). The evoked feedback EPSC burst in these INs was identical to the spontaneous SW-associated intracellular burst in the same cells (Figures 2D and 2G, Figure S3D). First, similar to the spontaneous SWi, evoked bursts were blocked by either GABAergic or glutamatergic antagonists. Second, within the evoked burst, successive EPSCs occurred at time-locked intervals of ~4 ms, similar to the pattern seen during SW-associated bursts (Figures 1H, 2D, and 2E; Figures S3A, S3B, and S3D). Third, evoked bursts had 4–6 summing EPSCs, with a peak amplitude of 1.0 ± 0.6 nA and time to peak of 16 ± 7 ms (n = 712 trials), similar to SWi bursts in which the same number of EPSCs summated to the peak in 16 ± 8 ms (Figure 2E). Fourth, spectral analysis shows that both events had the same frequency components (Figure 2E; Figures S3B and S3D). Fifth, in current clamp, evoked bursts drove INs to the threshold, with a high-frequency discharge of 3 ± 2 action potentials, and during spontaneous SWs, they discharged 2.5 ± 1.5 action potentials with a similar timing (Figures 2F and 2G). Notably, an evoked feedback burst was never observed in INs that did not show a feedback EPSC, suggesting that these INs are chandelier cells (Spampanato et al., 2016; Woodruff et al., 2006). Together, these data show that

evoked feedback EPSC bursts replicate SW-associated EPSC bursts and are likely driven by the same neural circuits. Consistent with this proposal, simultaneous LFP recording demonstrated that a feedback burst evoked by an action potential in a putative chandelier IN generated a SW in the extracellular LFP (Figure 2H;  $n = 3$ ) and a burst of IPSPs in local PNs (Figure S4;  $n = 8$ ) as seen during SWs (Figure 1) and was blocked by bicuculline (Figure 2H).

INs that displayed an evoked feedback burst were fast-spiking cells and predominantly encountered in the lateral and caudal BLA (Figure 3A). These INs expressed PV (Figure 3B) and had dendrites that were sparsely decorated with spines, and their axons formed a dense plexus within the BLA (Figures 3B and 3C; Figures S5A and S5B; Video S1). Consistent with previous studies (Woodruff et al., 2006; Spampanato et al., 2016), the axonal plexus of these INs contained numerous strings of pre-synaptic boutons or “cartridges” (Figure 3C) that made 2–6 synaptic contacts on the AIS of local PNs (Figure 3C;  $n = 7$ ), a defining feature of the axo-axonic chandelier cells (Muller et al., 2006; Somogyi et al., 1982; Howard et al., 2005; Veres et al., 2014).

Based on three fully recovered neurons, a single chandelier IN axon had  $166 \pm 46$  cartridge-type strings of pre-synaptic boutons, suggesting that each chandelier IN innervates well over 100 PNs at the AIS, the site with lowest threshold for action potential initiation (Kole and Stuart, 2012). These physiological and morphological characteristics of INs that evoked SWs identify these cells as PV-expressing chandelier INs.

We next tested the impact of silencing these cells on SWs. Genetic markers for that are specific for chandelier INs in the BLA are not available; thus, we turned to PV-Cre mice. Clozapine-N-oxide (CNO)-activated inhibitory designer receptors exclusively activated by designer drugs (DREADDi) were expressed in PV-INs by using adeno-associated virus. Whole-cell recordings from transduced INs identified, using m-Cherry fluorescence, confirmed the characteristic fast-spiking phenotype of PV-INs (Figure 3D), and exposure to CNO effectively hyperpolarized their membrane potential (Figure S5C) and reduced action potential discharge (Figure 3D; Figure S5D,  $n = 7$ ) and input resistance (Figure S5D,  $n = 7$ ,  $224 \pm 140$  MOhm versus  $183 \pm 137$  MOhm, paired t test p value, 0.0008). CNO had no effect on action potential generation or SWs in slices from control animals (data not shown), but in slices transduced with the inhibitory DREADDi, it significantly reduced the incidence of SW-associated synaptic events ( $n = 14$  slices; Figures 3E and 3F; Figures S5E and S5F). Silencing of PV INs not only reduced the SW-associated burst of GABAergic input to PNs ( $n = 7$ , Figure S5E) but also reduced the glutamatergic burst input to INs ( $n = 7$ ) (Figure 3E). Most PV-INs in the BLA are basket cells that provide strong somatic inhibition to PNs (McDonald and Bette, 2001; Woodruff and Sah, 2007); thus as expected, silencing PV-INs with CNO significantly reduced SW-associated inhibitory input to PNs. We have shown that action potentials in chandelier INs evoke disynaptic EPSCs with dual pharmacological sensitivity (Figure 2). Similar results have also been demonstrated in cortical chandelier INs (Molnár et al., 2008; Szabadics et al., 2006), and it has been suggested that GABA release at chandelier IN synapses recruits pyramidal neurons that drive feedback and feedforward glutamatergic inputs to INs (Molnár et al., 2008; Spampanato et al., 2016; Szabadics et

al., 2006; Woodruff et al., 2006). Thus, we suggest that the reduction of SW-associated glutamatergic input to INs results from silencing of PV chandelier INs.

### **PNs discharge sparsely with antidromically initiated action potentials**

We have shown that in the BLA, action potential discharge in a chandelier IN can initiate network activity that results in SWs. During this network activity, INs receive a summing excitatory input evoking a burst of action potentials, and PNs concurrently receive a summing GABAergic burst. To identify PNs that generate this excitatory synaptic activity, we bulk loaded brain slices with the calcium indicator Cal520 ( $n = 8$ ; STAR Methods). Two-photon imaging in these slices consistently showed spontaneous, correlated calcium transients, reporting action potential discharge in neurons (Figures 4A and 4B). The spontaneous calcium transients were correlated with SWs (Figures 4B and 4C), and although some neurons were active during every SW, others were silent or only fired occasionally (Figure 4B). Patch-clamp recording from neurons that discharged with every SW show that these cells were fast-spiking INs that expressed PV (Figure 4D), and neurons that were either silent or only occasionally active were PNs.

Glutamatergic neurons in the BLA are PNs (Sah et al., 2003), and these cells are extensively synaptically connected to local INs (Figure 6). Chandelier INs initiate SWs (Figures 2 and 3), during which INs receive a burst of glutamatergic EPSPs (Figures 1, 2, and 3; Figure S1; Figure 5), which are blocked by GABAA receptor antagonists. We have therefore suggested that some PNs must be driven to the threshold by GABAergic input from chandelier neurons. As chandelier INs innervate the AIS (Figure 3; Spampanato et al., 2016; Woodruff et al., 2006), PNs that discharge during SWs must be driven antidromically by axonal excitation (Glickfeld et al., 2009; Molnár et al., 2008; Spampanato et al., 2016; Szabadics et al., 2006; Woodruff et al., 2006).

To identify PNs discharging during SWs, we started with cell-attached recordings from PNs, thus leaving the intracellular milieu intact, and used high-resistance patch pipettes (12–15 M $\Omega$ ) to slow down intracellular dilution upon conversion to whole-cell mode. Consistent with the imaging data (Figure 4), cell-attached recordings revealed that some PNs (16/31 cells from 10 slices) intermittently discharged action potentials during SWs (Figures 4E and 4L). Action potentials that were time locked with SWs had an inflection in the rising phase, and the first order time derivative revealed two peaks with a prominent break between them (Figure 4F), consistent with initial segment (IS) and somato-dendritic (SD) components to the spike (Figures S6A-S6C; Colbert and Johnston, 1996; Coombs et al., 1957). Following conversion to whole-cell mode, 10/16 neurons continued to occasionally discharge action potentials for ~1–2 min (Figure 4G). These action potentials arose abruptly during the inhibitory burst (Figures 4G and 4H), with a spike threshold of  $-61 \pm 4$  mV (Figure 4L), and were followed by an after-depolarization (Figure 4I). Similar to cell-attached recordings, they had a striking inflexion in the rising phase and a large IS-SD break (Figure 4H). In contrast, action potentials evoked by somatic current injection ( $n = 10$ ) or by excitatory synaptic input ( $n = 4$ ) had a more depolarized spike threshold ( $-37 \pm 6$  mV) and a shorter IS-SD break and were followed by a fast after-hyperpolarization (Figures 4I-4K). The hyperpolarized spike threshold and longer IS-SD break of SW-associated action potentials

in PNs shows that these action potentials are driven antidromically (Böhner et al., 2011; Coombs et al., 1957; Hu et al., 2009) during the SW-associated burst of GABAergic input. Consistent with this, simultaneous extracellular patch-clamp recording from the soma and AIS of PNs confirmed that action potentials recorded during SWs are first seen in the AIS and then propagate to the soma (Figures S6C and S6D).

These results demonstrate that discharge of PNs during SWs is initiated by axonal excitation and preceded by GABAergic input. The engagement of PNs was sparse, with individual PNs discharging a single spike in ~40% of SWs (Figure 4L). In contrast, most INs (86%; 38/44) discharged action potentials time locked with SWs (Figure 1), with an engagement rate of  $81\% \pm 34\%$  (Figures 5A and 5B), and fired  $2.5 \pm 1.5$  action potentials at  $160 \pm 76$  Hz (Figures 5C and 5D). Most INs (>90%) that discharged a burst of action potentials during SWs were fast-spiking cells, characteristic of the PV INs. Confirming this, 15/15 INs recorded from slices made from PV EGFP mice discharged with every SWs. In contrast to PNs, SW-associated action potentials in INs were identical to those evoked by somatic current injection (Figures 5E and 5F), showing that they were initiated by dendritic synaptic input. Discharge of both INs and PNs began during the rising phase of the SW, with PN activity constrained almost entirely before the peak of the SW, whereas INs discharge began earlier and continued throughout the SW (Figure 5G). Together, these results demonstrate that in the BLA, although both PNs and INs participate in SWs, engagement of PNs is sparse, they are initiated antidromically, and engagement is limited to the early phase of the SW, whereas INs are driven orthodromically and most discharge throughout the SW envelope.

### Chandelier IN-driven circuit modules reproduce sharp waves

We have shown that in the BLA, an action potential in a chandelier IN can initiate network activity and SWs. This network activity is characterized as follows: (1) temporally organized burst of synaptic inputs in PNs and INs; (2) INs discharge with a burst of action potentials driven by a summing glutamatergic input; and (3) PNs receive a burst of inhibition, but a small number are driven to threshold by direct axonal excitation. As all recordings were made in acute brain slices, intrinsic circuits in BLA contain all the connections to generate SWs.

We next asked how BLA circuits are organized to generate SWs. To address this question, we first determined the properties of local synaptic connections between PNs, chandelier INs, and other INs. Chandelier INs were identified by the presence of evoked feedback EPSC (Figure 2B) that had an amplitude of  $218 \pm 158$  pA ( $n = 96$ ; Figure 6A). In 43 paired recordings between PNs and chandelier INs, 47% were connected and an action potential in the PN evoked an EPSC with an amplitude of  $161 \pm 108$  pA (Figure 6B), comparable to the size of evoked disynaptic feedback EPSC, showing that although chandelier neurons innervate many PNs, the evoked feedback EPSC originated from only 1–2 PNs. Of these pairs, 21% of PNs received a monosynaptic IPSP from the chandelier neuron and 26% were connected bidirectionally (Figure 6H). In two pairs, an action potential in the PN was able to drive the postsynaptic chandelier IN to the threshold (Figure 6E). As described above (Figure 2), this chandelier IN discharge evoked network activity, resulting in a feedback

EPSP burst in chandelier INs and large polysynaptic IPSP in the PN (Figure 6E,) showing that discharge from only a few PNs can initiate sustained network activity. PNs were also extensively connected to other INs (Figure 6F). From 15 pairs, 60% of INs were connected, in which an action potential in the PN evoked an EPSC of  $186 \pm 129$  pA ( $n = 9$ ).

Having determined the properties of IN-PN connections, we used this information to develop a network model for the BLA. This model contained 20,572 neurons with glutamatergic PNs making up 80% of the population, and the remainder comprised 2 types of INs, namely, chandelier INs (~2%) making axo-axonic synapses and other INs (~18%) making axo-somatic synapses on PNs (Bienvenu et al., 2012; McDonald and Bette, 2001; Spampinato et al., 2016; Veres et al., 2014; Figure 7A, top; Figure S7A). The network was configured as chandelier IN-driven modules (Figure 7A), with microcircuit structure and parameters including neuronal biophysical properties and synaptic strengths based on our experimental data (Figure S7; STAR Methods). Chandelier IN to PN connections were set as excitatory with log-normal distribution of synaptic weights (Figure S7C; Buzsáki and Mizuseki, 2014) that resulted in a single chandelier IN exciting only a small number of PNs, consistent with the amplitude of glutamatergic feedback events in our experimental data (Figures 6A-6D).

In this network model, action potential discharge in a chandelier IN initiated a burst of feedback EPSPs triggering time-locked action potentials in the same cells (Figure 7B). In voltage clamp, discharge in a chandelier IN initiated feedback EPSCs (Figure 7B) time locked at  $4.2 \pm 1$ -ms intervals that summated to a peak in  $19 \pm 3$  ms, reproducing the experimental data (Figure 2). This burst could be initiated by the chandelier IN exciting as few as two PNs (Figure 7C) and led to a cascade of events resulting in the generation of the extracellular SWs (Figure 7D), similar to those seen experimentally (Figure 1B and 4). This activity then propagated through the network by connected modules, generating multi-synaptic sequences of IPSCs in PNs and EPSCs in INs that summated in ~20 ms with an intrinsic frequency of 200–250 Hz (Figure 7E), reproducing the experimental data (Figures 1H-1J and 2B; Figure S3). The discharge of PNs was largely confined to the period before the SW peak paced by chandelier INs, whereas INs continued to discharge throughout the SW (Figures 7C and 7G), again reproducing our experimental data (Figure 5G).

In each cycle,  $4\% \pm 1\%$  PNs discharged with 1–2 action potentials, whereas  $32\% \pm 8\%$  of chandelier INs and  $42\% \pm 7\%$  of basket INs were active and burst fired 1–6 action potentials (Figures 7F-7H), again recreating the experimental data in Figures 2F, 4L, and 5C. These results indicate that the distribution of connection weights and synaptic efficacies between chandelier INs and PNs are finely tuned to enable chandelier IN-driven modules to generate the SW-population burst with only sparse discharge from PNs. Furthermore, activating specific chandelier INs in each trial resulted in the recruitment of a different set of PNs showing a unique spatial spread of population activity (Figure S7D). This finding indicates that discharges from different ensembles of PNs can generate SWs with the same temporal structure.

The temporal structure of SWs in the model originated from the circuit organization in chandelier-IN-driven modules and the distribution of synaptic weights in the network. In each module, a chandelier IN discharge evoked EPSC and IPSC sequences with successive disynaptic latencies of ~4 ms (Figure 7E), which summated in ~20 ms. The disynaptic latency resulted from synaptic delays, membrane time constants, and kinetics of AMPA and GABA<sub>A</sub> receptor currents. On the other hand, the summation latency of ~20 ms resulted solely from the log-normal distribution of synaptic weights, which together controls the balance of excitation and inhibition in the network. In support of the latter, an analytical model based on statistical distributions of connectivity and synaptic weights accurately predicted the observed summation latency (Figure S7E). Although the microcircuit parameters in the two different sets cited are known to affect disynaptic latencies and summation characteristics in general (Harris, 2005), our results reveal their differential roles in the generation of frequency components in SWs.

To elucidate the effect of the loss of microcircuits on SW generation, as happens in *ex vivo* slices, we sequentially reduced the size of the network model. The resulting chandelier-IN-evoked SW-bursts had a similar temporal structure but were associated with an overall reduction in the amplitude of synaptic bursts (Figure S8A). Together, simulations in the chandelier-IN-driven modules reliably reproduced experimental findings with high fidelity and showed resilience to the loss of microcircuits, as seen *ex vivo*.

In addition, simulations in the model predicated SW-associated synaptic events occur with a short lag of  $\pm 30$  ms between any two pairs of neurons (Figure S8B) and chandelier INs drive a feedforward SW burst of excitation in INs (Figure 7E). Consistent with these predictions, paired recordings ( $n = 24$ ) in BLA slices showed 96% of SWi had an onset lag with  $\pm 30$  ms (Figure S8B). Furthermore, paired recordings showed that discharge in a chandelier IN recruited INs reliably through time-locked feedforward SWi bursts of glutamatergic input ( $n = 2$ , Figure S8C), consistent with our interpretation of SWi-associated glutamatergic inputs shown in Figures 2 and 5. Silencing of basket INs in the model led to runaway excitation showing that axo-somatic inhibition plays a role in the termination of SWs (Figure S8D). However, due to lack of genetic tools to exclusively target basket INs, we could not test this prediction. Together, our simulation results show that circuits organized as chandelier-IN-controlled modules can reproduce SWs and accompanying cellular and synaptic activity with high fidelity entirely from local circuit mechanisms.

## DISCUSSION

Our results demonstrate that intrinsic circuits in the BLA generate SWs, during which INs and PNs receive temporally organized bursts of excitatory and inhibitory synaptic input, respectively. Action potential discharge in a chandelier IN is sufficient to initiate network activity, resulting in SWs. Simulations using a physiologically constrained network model with circuits organized as chandelier-IN-driven modules reproduced SWs with high fidelity. Our study provides a central role for chandelier INs in initiating SWs and a local circuit mechanism that explains their time course and termination.

Temporally organized activity in neural circuits generates oscillations in the extracellular field potential with distinct frequency bands that are associated with discrete cognitive functions (Buzsáki, 2006). This activity is present in many brain regions; however, our understanding of the circuit mechanisms that mediate different oscillations are limited (Harris, 2005). SWs are repetitive transitions in the LFP that have a low-frequency envelope lasting 50–100 ms, often with coupled high-frequency ripples (Buzsáki, 2015). These events have been described in several brain regions, including the amygdala, where they are thought to play a role in memory consolidation and retrieval (Buzsáki, 2015; Paré et al., 2002; Ponomarenko et al., 2003).

SWs were first described in the hippocampus *in vivo* (O'Keefe and Nadel, 1978) but are also seen in hippocampal slices *ex vivo* (English et al., 2014; Kubota et al., 2003; Maier et al., 2003). In the hippocampus, SWs within the CA1 region share many features to those in the BLA, as follows: (1) during each sharp wave, PNs and INs receive correlated bursts of GABAergic and glutamatergic synaptic input, respectively (Chiovini et al., 2014; Gan et al., 2017; Schlingloff et al., 2014); (2) they show dual pharmacological sensitivity to GABA<sub>A</sub> and AMPA receptor antagonists (Maier et al., 2003; Schlingloff et al., 2014); (3) sensitivity to targeted silencing of PV INs (Stark et al., 2014); and (4) during each SW, many INs discharge synchronously (Bazelot et al., 2016; Kubota et al., 2003; Maier et al., 2003), whereas PNs discharge sparsely with antidromic action potentials (Bähner et al., 2011).

A number of computational circuit models have suggested explanations for SWs in area CA1 of the hippocampus (Buzsáki, 2015; Figure S8E). Given the key role of GABAergic transmission during SWs, these models have suggested either reciprocal inhibition between INs (Maier et al., 2003), feedback inhibition (Ramirez-Villegas et al., 2018), a combination of reciprocal and feedback inhibition (Stark et al., 2014), or axo-axonic gap junctions (Draguhn et al., 1998) to explain SW generation. In the first three models, extrinsic inputs from CA3 are proposed to pace CA1 microcircuits and generate SWs. However, similar to our results in the BLA, experimental findings indicate that local circuits alone can generate SWs in the CA1 (Maier et al., 2011). In the fourth model, axo-axonic coupling between PNs is proposed as an intrinsic mechanism for SW generation, but evidence for such coupling remains contentious (reviewed in Buzsáki, 2015) and cannot explain the pharmacological sensitivity of SWs to GABA<sub>A</sub> antagonists. Although each of these models reproduces some aspects of SWs, local circuit mechanisms for the initiation, time course, and termination of these events are not addressed (reviewed in Buzsáki, 2015). Moreover, these models do not explain the resilience of microcircuits to generate SWs in the face of some damage, as occurs in *ex vivo* slice preparations.

In the BLA, we have shown that local network activity generates SWs, during which PNs and INs receive a correlated burst of inhibitory and excitatory input, respectively. These bursts have a stereotypical time course with time locked inputs at ~4-ms intervals that summate in a window of ~20 ms (Figures 1 and 2). This network activity, and the resultant SW, could be evoked by action potential discharge in a chandelier IN. We find that recruitment of PNs is sparse, and network activity during a SW is dominated by synchronous discharge of many INs. Simulations using a network model with circuits organized as chandelier-IN-driven modules reproduced the temporal structure of synaptic

events in SWs (Figure S8F). Importantly, this model explains the initiation and time course of SWs and accounts for its dual pharmacological sensitivity to GABA<sub>A</sub> and AMPA receptor antagonists that was fully conserved even with the loss of circuits, as in slices. Together, these findings reveal a resilient circuit organization, chandelier-IN-driven modules, that can generate oscillatory activity in neural networks with a consistent temporal structure.

Chandelier INs are a distinct class of PV-expressing INs that make synapses on the AIS (reviewed in Howard et al., 2005). Although these cells comprise a relatively small (<3%) proportion of the total IN pool, each chandelier IN innervates several hundred PNs (Howard et al., 2005; Woodruff et al., 2010). Their extensive axonal innervation and their strategic synaptic targeting of the AIS of PNs are ideally positioned to control synchronized activity in neural circuits (Howard et al., 2005; Woodruff et al., 2010). However, what functional role(s) these INs play network activity, if any, has been unclear. Our findings in the BLA show that action potentials in chandelier INs initiate SW by driving network activity with a specific temporal structure that engages both PNs and INs.

In the adult, GABAergic synapses are generally thought to be inhibitory (Ascoli et al., 2008; Glickfeld et al., 2009). However, GABAergic excitation of PNs by chandelier INs has been reported in the rodent BLA (Spampanato et al., 2016; Woodruff et al., 2006), cortex (Szabadics et al., 2006; Taniguchi et al., 2013), and hippocampus (Glickfeld et al., 2009) as well as human cortex (Molnár et al., 2008). The finding that PN discharge during SWs is driven antidromically is consistent with axo-axonic excitation of PNs by chandelier INs. In hippocampal CA1, PN discharge during SWs is also antidromic and enhanced by activation of axonal GABA<sub>A</sub> receptors (Bähner et al., 2011). Optogenetically driving PV INs has been reported to evoke SWs (Schlingloff et al., 2014; but see Stark et al., 2014), and silencing these INs in the BLA reduces SWs. In contrast to CA3, where chandelier INs are proposed to be inhibited in SWs (Viney et al., 2013), CA1 chandelier INs have been reported to discharge either during the early phase (Klausberger et al., 2003) or throughout SWs (Varga et al., 2014), suggesting the circuit mechanisms in CA3 might be different from those in CA1. The similarities between SWs in the BLA and the hippocampal CA1 region suggest similar circuit mechanisms and a potential role for PV-expressing chandelier INs in the generation of SWs in CA1.

In the hippocampus, SWs have long been associated with memory consolidation (Buzsáki, 2015). SWs are also present in the BLA *in vivo* (Ponomarenko et al., 2003), but their role in memory consolidation is not known. The BLA plays a central role in learning about aversive events (McGaugh, 2004; O'Neill et al., 2018; Pignatelli and Beyeler., 2019). *In vivo*, BLA chandelier INs are robustly recruited by noxious stimuli, and this activity has been proposed to synchronize PN ensembles to encode aversive information (Bienvenu et al., 2012). We have shown that in *ex vivo* slices, chandelier INs can drive large network activity to generate sharp waves. Although local networks are preserved in *ex vivo* slices, they are disconnected from a host of neuro-modulatory systems, and whether similar mechanisms operate *in vivo* and whether this mechanism contributes to learning about aversive events require further investigation.

## CONCLUSIONS

Sharp-wave ripples are oscillations seen in a number of brain regions and have been associated with memory consolidation and recall. SWs have been reported in the BLA *in vivo*, and here, we demonstrate that they are retained *ex vivo*. We show that chandelier INs in the BLA initiated SWs by recruiting PNs that drove temporally organized local network activity. We describe a network model organized as chandelier-IN-driven modules that fully reproduce SWs. These results demonstrate a functional role for chandelier INs in the BLA and a circuit mechanism for the generation of SWs that may shed light on the cellular and circuit dysfunction that underpins pathophysiological network activity seen in a range of neurological and mental disorders.

## STAR★METHODS

### RESOURCE AVAILABILITY

**Lead contact**—Further information regarding data, resources, and reagents should be directed to and will be fulfilled by the Lead Contact, Pankaj Sah (pankaj.sah@uq.edu.au)

**Materials availability**—This study did not generate any new materials or methods

**Data and code availability**—All data are available in the main text or the supplementary materials.

### EXPERIMENTAL MODEL AND SUBJECT DETAILS

All experimental and animal care procedures were conducted in accordance with the Australian Code of Practice for the Care and Use of Animals for Scientific Purposes and approved by the University of Queensland Animal Ethics Committee. *Animals*: Acute brain slices were prepared from 21-72 day old rats (Sprague Dawley or Wistar) and mice (wild-type (WT) or *heterozygous* transgenic) of either sex. Transgenic mice strains expressed enhanced green fluorescent protein (EGFP) under the control of Glutamate decarboxylase (GAD)-67 (C57BL/6NCrj x CBA/JNCrj) F1 or Parvalbumin (PV). Heterozygous PV-EGFP mouse colonies were established by crossing the transgenic PV-EGFP strain (Meyer et al., 2002) with WT mice (C57BL/6 and BALB/c background). For chemogenetic silencing experiments, transgenic PV::Cre knock in mouse strain (B6;129P2-Pvalb<sup>tm1(cre)Arbr/J</sup>) was used.

### METHOD DETAILS

**Electrophysiology**—Under isoflurane anesthesia, animals were perfused transcardially with ice-cold cutting artificial cerebrospinal fluid (ACSF) containing (in mM): 118 C<sub>5</sub>H<sub>14</sub>ClNO (choline chloride), 2.5 KCl, 2.5 CaCl<sub>2</sub>, 1.3 MgCl<sub>2</sub>, 1.2 NaH<sub>2</sub>PO<sub>4</sub>, 26 NaHCO<sub>3</sub> and 10 glucose, bubbled with carbogen (95% O<sub>2</sub>, 5% CO<sub>2</sub>), pH ~7.3, and osmolarity of 310-320 mOsm. The animal was then decapitated, the brain rapidly removed and submerged in ice-cold and carbogenated cutting ACSF. Following the removal of the cerebellum, the dorsal cerebrum was glued to a plate with a fronto-occipital angle ~10° and placed in a slicing chamber containing ice cold cutting ACSF continuously bubbled with carbogen

(95% O<sub>2</sub>, 5% CO<sub>2</sub>). Oblique horizontal slices were cut (400 μm) using a Vibratome (VT1000S, Leica, Germany) and transferred to a holding chamber designed-in-house with continuous circular perfusion of pre-warmed ACSF (in mM): 119 NaCl, 2.5 KCl, 2.5 CaCl<sub>2</sub>, 1.3 MgCl<sub>2</sub>, 1.2 NaH<sub>2</sub>PO<sub>4</sub>, 26 NaHCO<sub>3</sub> and 10 glucose, pH 7.3, Osmolarity ~300-320 mOsm and continuously bubbled with carbogen. Slices were allowed to recover for 1.5 – 2 h at physiological temperature (36-37°C) and subsequently stored at room temperature (24-26°C). After recovery, slices were transferred one at a time to a submerged type recording and imaging chamber perfused with carbogenated ACSF at 5-7 ml/min. In our hands, slices 275 μm thick, recovered at physiological temperature of ~36°C and maintained at high flow rate (5-7 mL/min) routinely showed network activity in the BLA. In addition, large temperature changes affected network activity in slices. Therefore, slices transferred within 1 h after incubation at 36-37°C were recorded at 33-34°C, and subsequent slices at 28-29°C.

Recording electrodes were fabricated from borosilicate glass pipettes (GC150F, 1.5 mm, Harvard Apparatus, UK) which when filled with whole-cell recording solution had a resistance of 3-6 MOhm. For some experiments, high resistance patch pipettes with 8-15 MOhm were used for whole cell patch recordings, to slow down intracellular dilution. Field electrodes were prepared using same borosilicate glass pipettes and, when filled with ACSF, had a resistance of 1-3 MOhm. For local electrical stimulation, bipolar glass electrodes were fabricated using borosilicate glass pipettes ((TGC150-7.5, 1.5 mm, Harvard Apparatus, UK) and filled with ACSF. For whole-cell and cell-attached extracellular recordings, patch electrodes were filled with (in mM): 135 KMeSO<sub>4</sub>, 7 NaCl, 10 HEPES, 2 Mg<sub>2</sub>ATP, 0.3 Na<sub>2</sub>GTP, 10 EGTA or no EGTA and 0.3% biocytin, pH 7.3 and 280-290 mOsm. For local field potential (LFP) recordings, the field electrode was filled with ACSF, 150 mM NaCl, or 1M NaCl. Pharmacological reagents were dissolved in water or DMSO, diluted in ACSF, and perfused into the recording chamber. Concentration of reagents for bath-application: bicuculline (2 or 10 μM, Tocris), picrotoxin (100 μM, Sigma-Aldrich), Gabazine (10 μM, Tocris), 2,3-Dioxo-6-nitro-1,2,3,4-tetrahydrobenzo [*f*] quinoxaline-7-sulfonamide (NBQX, 10 μM, Tocris), 6-Cyano-7-nitroquinoxaline-2,3-dione (CNQX, 10 or 15 μM, Tocris) and Clozapine-N-oxide (CNO, 5, 10 or 30 μM, AK Scientific).

Slices were visualized under an upright microscope, either an (1) Olympus-BX50WI fitted with Infrared differential interference contrast, 40X water immersion objective and a fluorescent lamp (Olympus U RFLT, Olympus Optical) or (2) an Axio Examiner Z1 fitted with Dodt gradient contrast, 40X (Zeiss, Germany) or 60X (Olympus) immersion objective and a fluorescent lamp (X-cite 120Q, Excelitas). Neurons were imaged with a camera either IR-1000 (Dagemti, USA), ProgRes (Jenoptik, Germany) or Retiga Electro (QImaging, Canada). Electrical signals were acquired with a Multiclamp 700A and 700B amplifier (Molecular Devices, USA), digitized using ITC-16 A/D converter (InstruTECH, Germany), and recorded using Axograph X (Axograph Scientific, USA). Cellular electrical signals were acquired from DC –10 kHz and digitized at 40-60 kHz. Intracellular voltage signals were not corrected for liquid junction potential. LFP were acquired with a Bessel filter set at 1 Hz - 1 KHz and digitized at 5-60 kHz with x2000 amplification. For LFP signal, the mains interference (50 Hz) was removed using Humbug (Digitimer, UK). *Post hoc* data analysis was performed with Axograph, and MATLAB (MathWorks, USA). Numerical calculations

and graphs were prepared with Microsoft Excel (Microsoft, USA) and Prism (version 6 and 7, GraphPad Software Inc, USA).

In oblique horizontal slices, the basolateral amygdala (BLA) was distinguished as a triangular region demarcated medially and laterally by fiber bundles, and caudally by the lateral ventricle and hippocampus. Under visual guidance using differential interference contrast or Dodt contrast and video camera, cell-attached and whole-cell recordings were obtained from single neurons. In slices obtained from transgenic mice, interneurons (INs) were targeted using EGFP fluorescence illuminated from a fluorescent lamp and dichroic filter (495 nm). Cell-attached extracellular recordings obtained from somata had a seal resistance  $> 1$  GOhm. Whole-cell recordings had a series resistance from 5-30 MOhm and the Bridge balance was manually adjusted. Neurons were injected with a step current injection for 600 ms ( $-50$  pA to  $820$  pA,  $30$  pA steps) to determine intrinsic action potential discharge properties. Using previously reported electrophysiological classification of neurons in BLA (Rainnie et al., 1993; Woodruff and Sah, 2007), we classified principal neurons (PNs) and interneurons (INs) based on the action potential discharge patterns and width at half maximal amplitude of the action potential (half-width). Action potentials elicited with supra-threshold ( $120$  pA, 3 steps) above threshold step was used for classification of firing discharge of INs. The amplitude and half-width were measured from the first action potential discharged with current injection steps. Input resistance ( $R_{in}$ ) was calculated from the change in membrane potential ( $V_m$ ) elicited with a current pulse of  $-50$  pA ( $I$ ) for  $50$  ms. Input resistance ( $R_{in}$ ) was calculated post hoc from  $V_m$  using *Ohm's law*:  $R_{in} = V_m/I$ . In some experiments, loose cell-attached extracellular recordings were obtained from the axon initial segment close to the soma using a patch pipette filled with  $150$  mM NaCl or ACSF. The axon initial segment ( $\sim 30$   $\mu$ m) from the soma was identified using a  $4X$  magnified  $60x$  DIC image and verified using electrical coupling of action potential discharge between the soma and axon, and subsequently verified with filling the soma with fluorescent Alexa 594 added in the intracellular patch solution and imaged under two-photon excitation at  $800$  nm. The resting membrane potentials (RMPs) of both PNs and INs ( $-65$  to  $-75$  mV) were more negative than the chloride reversal potential ( $-60$  mV) of the whole-cell patch electrode solution. Field electrodes were placed in the BLA to recorded spontaneous sharp-wave oscillations (SWs) in the local field potential (LFP). Cellular activity was monitored for intracellular synaptic events in SWs (SWi) and action potential discharge from neurons  $100$ - $300$   $\mu$ m from the field electrode. *Principal neurons (PNs)*: In PNs, SW-associated post-synaptic currents were recorded in voltage-clamp configuration from holding potential of  $-70$  mV to  $-50$  mV and  $5$  mV steps. The AP discharge in PNs in SWs was recorded extracellularly on the soma using a high resistance cell-attached patch electrode (seal resistance  $\sim 1$  GOhm) and subsequently converted to whole-cell configuration (seal resistance  $\sim 40$  MOhm). *Evoked orthodromic APs*: To evaluate AP waveform by orthodromic excitatory inputs, a stimulating electrode was placed on the external capsule axon bundle on the lateral side and whole-cell recordings were obtained from BLA PNs in presence of GABA<sub>A</sub> receptor antagonist (gabazine). Stimulation of axon bundle for  $0.1$  ms at  $\sim 0.1$  Hz excitatory post-synaptic potential evoked APs. After each experiment, AMPA receptor antagonist (CNQX) was bath applied to verify stimulation evoked orthodromic AP through glutamatergic inputs. *Dual recordings in*

*single neurons*: Dual recordings were simultaneously obtained from a single PN soma with cell-attached extracellular patch electrode and a whole-cell intracellular patch electrode. Intracellular current injection elicited action potential discharges were recorded concurrently by whole-cell and cell-attached electrodes. In a subset of experiments, dual recordings were obtained from soma (whole-cell or cell-attached) and axon initial segment (loose cell-attached) of PNs to record somatic and axonal components of the action potential.

*Interneurons (INs)*: In INs, SW associated intracellular (SWi) post-synaptic currents were recorded in voltage-clamp configuration from a holding potential of  $-70$  mV. In current clamp, the action potential discharge in SWs were recorded in whole cell configuration. All INs were verified for evoked feedback excitation. In voltage clamp, a single action potential 'unclamped current' was triggered using a brief voltage step pulse of  $+70$  mV for  $0.5$  ms from a holding potential of  $-70$  mV and monitored for time-locked feedback excitatory post-synaptic currents (EPSCs). Similarly, in current clamp, a single action potential was triggered with a brief square pulse of  $2$ - $2.5$  nA for  $0.5$  ms and monitored for time-locked feedback excitatory post-synaptic potentials (EPSPs). To allow synaptic recovery, these trials were repeated at  $3.5$  s intervals. Initially, INs were randomly sampled and monitored for single discharge evoked feedback excitation for a minimum of  $30$  trials. INs with time-locked disynaptic feedback excitation were classified as chandelier INs (Woodruff et al., 2006; Szabadics et al., 2006; Molnár et al., 2008; Taniguchi et al., 2013; Spampanato et al., 2016) and monitored for evoked feedback burst and SWi. After morphological reconstructions, we preferentially targeted INs with thick bifurcating dendrite near the soma to increase yield of chandelier INs (typically 1 out of 4 cells). INs with no feedback were either monitored for SW associated burst activity or discontinued immediately. *Synaptic connections*: Paired recordings were obtained between randomly selected neurons that were  $\sim 100$  microns apart from each other in a medio-lateral or rostrocaudal directions. To identify synaptic connections in paired recordings, an action potential was evoked in the first (pre-synaptic) neuron and synaptic responses were recorded in the second (post-synaptic) neuron in current clamp and voltage-clamp configurations, and then repeated in the opposite direction. Monosynaptic EPSCs and IPSCs were recorded with the post-synaptic neuron held at  $-70$  mV and  $-50$  mV, respectively. Averages of  $10$  or more trials were used to measure synaptic connections.

**Multi-cell bolus loading of the fluorescent indicator Cal-520 AM**—Spike-triggered  $\text{Ca}^{2+}$  activity was imaged using the fluorescent  $\text{Ca}^{2+}$  indicator Cal- 520 AM (Abcam). Multi-cell bolus loading was performed by spot loading. Cal- 520 AM stock ( $2$  mM) was prepared in DMSO and aliquoted as  $7$   $\mu\text{l}$  units. Before each experiment, an aliquot of stock was thawed and diluted with freshly made DMSO containing  $10\%$  pluronic acid to  $1.4$  mM ( $10$   $\mu\text{l}$ ), then sonicated for  $3$ - $5$  min. The sonicated Cal-520 AM mix was diluted with  $30$   $\mu\text{l}$  of filtered loading solution containing (in mM):  $147.5$  NaCl,  $2.5$  KCl and  $10$  HEPES, pH  $7.3$  to make a spot loading solution with a final concentration of Cal-520 AM of  $0.35$  mM ( $40$   $\mu\text{l}$ ). The spot loading solution was sonicated for  $3$ - $5$  min. Individual slices were transferred to a recording chamber. For spot loading, we used the electrophysiology patch electrode set-up connected with a manometer and a  $5$  mL syringe. A patch glass pipette filled with the spot loading solution was inserted into the slice and a positive pressure of  $10$ - $15$  psi pressure was applied for  $1$ - $3$  min. Subsequently, the patch electrode was slowly removed,

and the slice was allowed to recover for 30 min in the recording chamber. After 30 minutes, the slice was verified for Cal-520 loaded somata using a two-photon excitation laser (800 nm). *Spike-triggered  $Ca^{2+}$  activity imaged with Cal-520 AM fluorescent transients (CaTs):* In each slice, Cal-520 loaded somata in the BLA (~200 X 200 micron<sup>2</sup>) were excited with a two-photon laser at 800 nm (Coherent, USA) under a 40 X objective using an Axio Examiner Z1 microscope (Zeiss, Germany) and emission was detected with non-descanned detectors (Zeiss, Germany), and acquired with a Zen software package (Zen 2012, USA) at ~3.5 Hz. To identify spontaneous population activity online, regions of interest (ROIs) were placed on the somata and the change in fluorescence was monitored using the Zen software package. CaTs were captured from loaded slices along with electrical recording for SWs in the imaging area. In a subset of experiments, somata with transients in SWs were then targeted with patch recordings to verify the action potential discharge with CaTs.

**Viral injection**—Transgenic PV::Cre mice (21-28 days old) were anesthetized with intraperitoneal ketamine (100 mg/kg), and xylazine (10 mg/kg), then placed in a stereotaxic frame. The BLA was targeted bilaterally using the following co-ordinates: antero-posterior -1.8 mm, medio-lateral 3 mm and dorso-ventral from the skull 4.8 mm. A small burr hole was made and the viral construct - EF1a-DIO-hM4D(Gi-mCherry with serotype AAV1/2 and AAV2 (adeno-associated virus, titer:  $2.7 \times 10^{12}$  GC/ml, volume of injection: 1  $\mu$ l) was delivered into the BLA using a Picospritzer III (10-30 psi, 10-20 ms). After injection, mice were quarantined for 48 hours and allowed to recover for at least 3 weeks. After 3 weeks, brain slices were prepared as described above, verified for infected cells with mCherry fluorescence in somata in the BLA under laser excitation (561 nm) and electrophysiological recordings obtained as described above.

**Immunohistochemistry and morphological reconstruction**—During whole-cell patch recording, neurons were filled with biocytin and neuronal morphology was recovered by immunolabeling for biocytin. After recording, slices were transferred to a 16 well plate with 4% paraformaldehyde (PFA) in 0.1 M phosphate buffered saline (PBS), pH 7.2, incubated for 1 h at room temperature for rapid fixation and then transferred to a cold room (4 C) for overnight incubation. On the following day, the PFA fixed slices were resuspended in 0.1 M PBS and rinsed 3 times for 15 min. The slices were subsequently submerged in blocking buffer: 1% BSA, 0.05% saponin, and 0.05% sodium azide in 0.1M PBS, and incubated on a shaker for 1h at room temperature. To label biocytin, Alexa Fluor -555/647 bound to streptavidin (1:2000, Invitrogen) was added to the blocking buffer and incubated overnight at room temperature. On the following day, the blocking buffer was removed, and the slices were washed with 0.1 M PBS, 3 times for 15 min, and then mounted on a glass slide with DABCO. Immunolabeled neurons were verified under an upright fluorescence microscope (Axio Imager, Zeiss) and imaged with the spinning-disk confocal system (Marianas; 3I, Inc.) consisting of a Axio Observer Z1 (Carl Zeiss) equipped with a CSU-W1 spinning-disk head (Yokogawa Corporation of America), ORCA-Flash4.0 v2 CMOS camera (Hamamatsu Photonics), 20x 0.8 NA PlanApo and 40x 1.2 NA C-Apo objectives. Image acquisition was performed using SlideBook 6.0 (3I, Inc).

**Immunolabeling for synaptic contacts**—After imaging, slices were embedded in 4% agarose and sub-sectioned to 70 microns thick slabs using a vibratome (VT1000S vibratome, Leica). Sub-sectioned slices were suspended in the same blocking buffer as described above with primary antibodies for parvalbumin (mouse anti-parvalbumin, 1:2000, Sigma-Aldrich) and Ankyrin-G (rabbit anti-Ankyrin G, 1:500, Santa Cruz) and incubated at room temperature for two days. The blocking buffer was removed after 2 days and slices were washed with 0.1M PBS, 3 times for 15 minutes. Then, they were resuspended with blocking buffer containing secondary antibodies conjugated with fluorophores: goat anti-mouse, Alexa 405 (1:1000, Life Technologies) and goat anti-rabbit, Alexa Fluor 647(1:1000, Invitrogen) for 1 day at room temperature. On the following day, slices were washed with 0.1 M PBS, 3X for 15 min and mounted on glass slides with DABCO. Synaptic contacts were imaged with 63X and 100X oil immersion objectives using the imaging set-up described above. *Morphological reconstruction*: Biocytin-labeled neurons imaged before sub-sectioning were manually traced using NeuroLucida-360 (MBF Bioscience) and visualized in NeuroExplorer (MBF Bioscience). In recovered chandelier neurons, strings of pre-synaptic ‘cartridge’ boutons were analyzed using Fiji (ImageJ).

**Data analysis**—*LFP analysis*. Wide-band LFP signals were filtered for sharp-wave-ripple (SWs) frequency bands using in-built bandpass filters in Axograph. To generate spectrograms, the wide-band LFP signal was detected for SWs using the amplitude criteria and event detection function in Axograph. Detected events were captured, verified manually, and aligned to the peak with a  $\pm 400$  ms data window referenced to the peak. Spectrograms were generated using captured wide-band LFP signals and lab-written routines in MATLAB. *SW-associated synaptic events*: SW-associated intracellular post-synaptic currents (SWi PSCs) were ~10-15 fold larger than monosynaptic events and were captured using the amplitude criteria and event detection function in Axograph and verified visually. Captured episodes were aligned at the peak with a data window of  $\pm 400$  ms. SWi PSCs in PNs (holding potential  $-50$  mV) and in INs (holding potential  $-70$  mV) were analyzed for onset, time to reach peak amplitude and peak amplitude. The time to peak amplitude was calculated as the difference between the onset and location of the peak amplitude for each episode. Spectrograms of captured SW-associated PSCs were prepared using lab-written routines in MATLAB. *SW action potential discharge analysis*: Intracellularly recorded action potentials were analyzed for threshold membrane potential, defined as the membrane potential ( $V_m$ ) when the first derivative ( $dV/dt$ ) reached 50 mV/ms. The latency between the initial segment and somato-dendritic components was measured as a time difference between two peaks in the second order time-derivative of action potentials recorded in whole-cell configuration and the first order time-derivative of action potentials recorded in cell-attached configuration. In INs, action potentials recorded intracellularly were analyzed for latency to discharge from the onset of SW input and number of action potentials in each episode. The action potential discharge probability of PNs and INs in SW was calculated from timing of action potential discharge ( $\pm 150$  ms, 4 ms bins) with reference to peak of SW (1-20 Hz), for each cell. Probability was calculated by dividing the number of action potentials in each bin window by the total number of SW episodes. *INs with feedback excitation*: Voltage-clamp recordings for INs evoked feedback burst EPSCs were analyzed for time-interval between EPSCs in each episode. Spectral analysis of evoked

feedback EPSC bursts was obtained using Fast Fourier Transform (FFT in Axograph) for a time-window of 60 ms from the onset of feedback. Spectrograms of evoked feedback bursts were prepared using lab-written routines in MATLAB. In current clamp, IN evoked feedback bursts of excitatory post-synaptic potentials were analyzed for timing of action potential discharge and inter-spike intervals. *Spike-triggered  $Ca^{2+}$  transient (CaT) analysis*: Fluorescence was measured as a ratio of change in fluorescence to baseline fluorescence ( $F/F_0\%$ ) in Axograph. CaTs were detected using the simple threshold method.

## QUANTIFICATION AND STATISTICAL ANALYSIS

Data are reported as cumulative/relative frequencies and summarized as median or mean standard deviation as indicated. The ‘n’ values reported in the results and figures represent the number of episodes/cells/trials/slices as indicated. Parametric tests were used if values passed a normality test, otherwise a non-parametric test was applied. A *P value* < 0.05 was considered significant. Grubb’s test was used to identify outliers before statistical tests.

## Supplementary Material

Refer to Web version on PubMed Central for supplementary material.

## ACKNOWLEDGMENTS

P.Sah. was supported by grants from the Australian National Health and Medical Research Council and the Australian Research Council (CE140100007). B.L. was supported by US National Science Foundation Graduate Research Fellowship; S.N. was supported by grant 15 NIH MH122023. We thank Stephen Williams, Alan Woodruff, Petra Sedlak, Rowan Tweedale, Paul Marshall, Esmi Zajackowski, and John Morris for commenting on the manuscript and the QBI microscopy suite for help with microscopy.

## REFERENCES

- Alturki A, Feng F, Nair A, Guntu V, and Nair SS (2016). Distinct current modules shape cellular dynamics in model neurons. *Neuroscience* 334, 309–331. [PubMed: 27530698]
- Ascoli GA, Alonso-Nanclares L, Anderson SA, Barrionuevo G, Benavides-Piccione R, Burkhalter A, Buzsáki G, Cauli B, Defelipe J, Fairén A, et al. ; Petilla Interneuron Nomenclature Group (2008). Petilla terminology: nomenclature of features of GABAergic interneurons of the cerebral cortex. *Nat. Rev. Neurosci* 9, 557–568. [PubMed: 18568015]
- Axmacher N, Mormann F, Fernández G, Elger CE, and Fell J (2006). Memory formation by neuronal synchronization. *Brain Res. Brain Res. Rev* 52, 170–182.
- Bähner F, Weiss EK, Birke G, Maier N, Schmitz D, Rudolph U, Frotscher M, Traub RD, Both M, and Draguhn A (2011). Cellular correlate of assembly formation in oscillating hippocampal networks in vitro. *Proc. Natl. Acad. Sci. USA* 108, E607–E616. [PubMed: 21768381]
- Bazelot M, Teleczuk MT, and Miles R (2016). Single CA3 pyramidal cells trigger sharp waves in vitro by exciting interneurons. *J. Physiol* 594, 2565–2577. [PubMed: 26728572]
- Bienvenu TC, Busti D, Magill PJ, Ferraguti F, and Capogna M (2012). Cell-type-specific recruitment of amygdala interneurons to hippocampal theta rhythm and noxious stimuli in vivo. *Neuron* 74, 1059–1074. [PubMed: 22726836]
- Bocchio M, Nabavi S, and Capogna M (2017). Synaptic Plasticity, Engrams, and Network Oscillations in Amygdala Circuits for Storage and Retrieval of Emotional Memories. *Neuron* 94, 731–743. [PubMed: 28521127]
- Buzsáki G (2006). *Rhythms of the Brain* (Oxford University Press).
- Buzsáki G (2015). Hippocampal sharp wave-ripple: A cognitive biomarker for episodic memory and planning. *Hippocampus* 25, 1073–1188. [PubMed: 26135716]

- Buzsáki G, and Mizuseki K (2014). The log-dynamic brain: how skewed distributions affect network operations. *Nat. Rev. Neurosci* 15, 264–278. [PubMed: 24569488]
- Buzsáki G, Horváth Z, Urioste R, Hetke J, and Wise K (1992). High-frequency network oscillation in the hippocampus. *Science* 256, 1025–1027. [PubMed: 1589772]
- Carnevale NT, and Hines ML (2006). *The NEURON book* (Cambridge University Press).
- Chiovini B, Turi GF, Katona G, Kaszás A, Pálfi D, Maák P, Szalay G, Szabó MF, Szabó G, Szadai Z, et al. (2014). Dendritic spikes induce ripples in parvalbumin interneurons during hippocampal sharp waves. *Neuron* 82, 908–924. [PubMed: 24853946]
- Chung L, and Moore SD (2009). Neuropeptides modulate compound post-synaptic potentials in basolateral amygdala. *Neuroscience* 164, 1389–1397. [PubMed: 19786076]
- Colbert CM, and Johnston D (1996). Axonal action-potential initiation and Na<sup>+</sup> channel densities in the soma and axon initial segment of subicular pyramidal neurons. *J. Neurosci* 16, 6676–6686. [PubMed: 8824308]
- Coombs JS, Curtis DR, and Eccles JC (1957). The interpretation of spike potentials of motoneurons. *J. Physiol* 139, 198–231. [PubMed: 13492209]
- Csicsvari J, Hirase H, Mamiya A, and Buzsáki G (2000). Ensemble patterns of hippocampal CA3-CA1 neurons during sharp wave-associated population events. *Neuron* 28, 585–594. [PubMed: 11144366]
- Destexhe A, Mainen ZF, and Sejnowski TJ (1994). An Efficient Method for Computing Synaptic Conductances Based on a Kinetic-Model of Receptor-Binding. *Neural Comput.* 6, 14–18.
- Draguhn A, Traub RD, Schmitz D, and Jefferys JG (1998). Electrical coupling underlies high-frequency oscillations in the hippocampus in vitro. *Nature* 394, 189–192. [PubMed: 9671303]
- Durstewitz D, Seamans JK, and Sejnowski TJ (2000). Dopamine-mediated stabilization of delay-period activity in a network model of prefrontal cortex. *J. Neurophysiol* 83, 1733–1750. [PubMed: 10712493]
- Einevoll GT, Kayser C, Logothetis NK, and Panzeri S (2013). Modelling and analysis of local field potentials for studying the function of cortical circuits. *Nat. Rev. Neurosci* 14, 770–785. [PubMed: 24135696]
- English DF, Peyrache A, Stark E, Roux L, Vallentin D, Long MA, and Buzsáki G (2014). Excitation and inhibition compete to control spiking during hippocampal ripples: intracellular study in behaving mice. *J. Neurosci* 34, 16509–16517. [PubMed: 25471587]
- Feng F, Samarth P, Paré D, and Nair SS (2016). Mechanisms underlying the formation of the amygdalar fear memory trace: A computational perspective. *Neuroscience* 322, 370–376. [PubMed: 26944604]
- Galarreta M, and Hestrin S (1997). Properties of GABAA receptors underlying inhibitory synaptic currents in neocortical pyramidal neurons. *J. Neurosci* 17, 7220–7227. [PubMed: 9295368]
- Gan J, Weng SM, Pernía-Andrade AJ, Csicsvari J, and Jonas P (2017). Phase-Locked Inhibition, but Not Excitation, Underlies Hippocampal Ripple Oscillations in Awake Mice In Vivo. *Neuron* 93, 308–314. [PubMed: 28041883]
- Glickfeld LL, Roberts JD, Somogyi P, and Scanziani M (2009). Interneurons hyperpolarize pyramidal cells along their entire somatodendritic axis. *Nat. Neurosci* 12, 21–23. [PubMed: 19029887]
- Gold C, Henze DA, Koch C, and Buzsáki G (2006). On the origin of the extracellular action potential waveform: A modeling study. *J. Neurophysiol* 95, 3113–3128. [PubMed: 16467426]
- Goto T, Hatanaka R, Ogawa T, Sumiyoshi A, Riera J, and Kawashima R (2010). An evaluation of the conductivity profile in the somatosensory barrel cortex of Wistar rats. *J. Neurophysiol* 104, 3388–3412. [PubMed: 20810682]
- Harris KD (2005). Neural signatures of cell assembly organization. *Nat. Rev. Neurosci* 6, 399–407. [PubMed: 15861182]
- Hauffler D, and Pare D (2014). High-frequency oscillations are prominent in the extended amygdala. *J. Neurophysiol* 112, 110–119. [PubMed: 24717353]
- Howard A, Tamas G, and Soltesz I (2005). Lighting the chandelier: new vistas for axo-axonic cells. *Trends Neurosci.* 28, 310–316. [PubMed: 15927687]

- Hu W, Tian C, Li T, Yang M, Hou H, and Shu Y (2009). Distinct contributions of Na(v)1.6 and Na(v)1.2 in action potential initiation and backpropagation. *Nat. Neurosci* 12, 996–1002. [PubMed: 19633666]
- Hummos A, Franklin CC, and Nair SS (2014). Intrinsic mechanisms stabilize encoding and retrieval circuits differentially in a hippocampal network model. *Hippocampus* 24, 1430–1448. [PubMed: 24978936]
- Joo HR, and Frank LM (2018). The hippocampal sharp wave-ripple in memory retrieval for immediate use and consolidation. *Nat. Rev. Neurosci* 19, 744–757. [PubMed: 30356103]
- Kim D, Paré D, and Nair SS (2013). Mechanisms contributing to the induction and storage of Pavlovian fear memories in the lateral amygdala. *Learn. Mem* 20, 421–430. [PubMed: 23864645]
- Klausberger T, Magill PJ, Márton LF, Roberts JDB, Cobden PM, Buzsáki G, and Somogyi P (2003). Brain-state- and cell-type-specific firing of hippocampal interneurons *in vivo*. *Nature* 421, 844–848. [PubMed: 12594513]
- Kole MH, and Stuart GJ (2012). Signal processing in the axon initial segment. *Neuron* 73, 235–247. [PubMed: 22284179]
- Kubota D, Colgin LL, Casale M, Brucher FA, and Lynch G (2003). Endogenous waves in hippocampal slices. *J. Neurophysiol* 89, 81–89. [PubMed: 12522161]
- Li G, Nair SS, and Quirk GJ (2009). A biologically realistic network model of acquisition and extinction of conditioned fear associations in lateral amygdala neurons. *J. Neurophysiol* 101, 1629–1646. [PubMed: 19036872]
- Magee J, Hoffman D, Colbert C, and Johnston D (1998). Electrical and calcium signaling in dendrites of hippocampal pyramidal neurons. *Annu. Rev. Physiol* 60, 327–346. [PubMed: 9558467]
- Mahanty NK, and Sah P (1998). Calcium-permeable AMPA receptors mediate long-term potentiation in interneurons in the amygdala. *Nature* 394, 683–687. [PubMed: 9716132]
- Maier N, Nimmrich V, and Draguhn A (2003). Cellular and network mechanisms underlying spontaneous sharp wave-ripple complexes in mouse hippocampal slices. *J. Physiol* 550, 873–887. [PubMed: 12807984]
- Maier N, Tejero-Cantero A, Dorn AL, Winterer J, Beed PS, Morris G, Kempter R, Poulet JF, Leibold C, and Schmitz D (2011). Coherent phasic excitation during hippocampal ripples. *Neuron* 72, 137–152. [PubMed: 21982375]
- McDonald AJ, and Betette RL (2001). Parvalbumin-containing neurons in the rat basolateral amygdala: morphology and co-localization of Calbindin-D(28k). *Neuroscience* 102, 413–425. [PubMed: 11166127]
- McGaugh JL (2004). The amygdala modulates the consolidation of memories of emotionally arousing experiences. *Annu. Rev. Neurosci* 27, 1–28. [PubMed: 15217324]
- Meyer AH, Katona I, Blatow M, Rozov A, and Monyer H (2002). *In vivo* labeling of parvalbumin-positive interneurons and analysis of electrical coupling in identified neurons. *J. Neurosci* 22, 7055–7064. [PubMed: 12177202]
- Migliore M, Hoffman DA, Magee JC, and Johnston D (1999). Role of an A-type K<sup>+</sup> conductance in the back-propagation of action potentials in the dendrites of hippocampal pyramidal neurons. *J. Comput. Neurosci* 7, 5–15. [PubMed: 10481998]
- Molnár G, Oláh S, Komlósi G, Füle M, Szabadics J, Varga C, Barzó P, and Tamás G (2008). Complex events initiated by individual spikes in the human cerebral cortex. *PLoS Biol.* 6, e222. [PubMed: 18767905]
- Muller JF, Mascagni F, and McDonald AJ (2006). Pyramidal cells of the rat basolateral amygdala: synaptology and innervation by parvalbumin-immunoreactive interneurons. *J. Comp. Neurol* 494, 635–650. [PubMed: 16374802]
- O’Keefe J, and Nadel L (1978). *The Hippocampus as a Cognitive Map* (Oxford University Press).
- O’Neill PK, Gore F, and Salzman CD (2018). Basolateral amygdala circuitry in positive and negative valence. *Curr. Opin. Neurobiol* 49, 175–183. [PubMed: 29525574]
- Pape HC, Paré D, and Driesang RB (1998). Two types of intrinsic oscillations in neurons of the lateral and basolateral nuclei of the amygdala. *J. Neurophysiol* 79, 205–216. [PubMed: 9425192]

- Parasuram H, Nair B, D'Angelo E, Hines M, Naldi G, and Diwakar S (2016). Computational Modeling of Single Neuron Extracellular Electric Potentials and Network Local Field Potentials Using LFPsim. *Front. Comput. Neurosci* 10, 65. [PubMed: 27445781]
- Paré D, Collins DR, and Pelletier JG (2002). Amygdala oscillations and the consolidation of emotional memories. *Trends Cogn. Sci* 6, 306–314. [PubMed: 12110364]
- Pignatelli M, and Beyeler A (2019). Valence coding in amygdala circuits. *Curr. Opin. Behav. Sci* 26, 97–106. [PubMed: 32832584]
- Polepalli JS, Gooch H, and Sah P (2020). Diversity of interneurons in the lateral and basal amygdala. *NPJ Sci. Learn* 5, 10. [PubMed: 32802405]
- Ponomarenko AA, Korotkova TM, and Haas HL (2003). High frequency (200 Hz) oscillations and firing patterns in the basolateral amygdala and dorsal endopiriform nucleus of the behaving rat. *Behav. Brain Res* 141, 123–129. [PubMed: 12742248]
- Popescu AT, and Paré D (2011). Synaptic interactions underlying synchronized inhibition in the basal amygdala: evidence for existence of two types of projection cells. *J. Neurophysiol* 105, 687–696. [PubMed: 21084688]
- Power JM, Bocklisch C, Curby P, and Sah P (2011). Location and function of the slow afterhyperpolarization channels in the basolateral amygdala. *J. Neurosci* 31, 526–537. [PubMed: 21228162]
- Rainnie DG (1999). Serotonergic modulation of neurotransmission in the rat basolateral amygdala. *J. Neurophysiol* 82, 69–85. [PubMed: 10400936]
- Rainnie DG, Asproдини EK, and Shinnick-Gallagher P (1993). Intracellular recordings from morphologically identified neurons of the basolateral amygdala. *J. Neurophysiol* 69, 1350–1362. [PubMed: 8492168]
- Rainnie DG, Mania I, Mascagni F, and McDonald AJ (2006). Physiological and morphological characterization of parvalbumin-containing interneurons of the rat basolateral amygdala. *J. Comp. Neurol* 498, 142–161. [PubMed: 16856165]
- Ramirez-Villegas JF, Willeke KF, Logothetis NK, and Besserve M (2018). Dissecting the Synapse- and Frequency-Dependent Network Mechanisms of In Vivo Hippocampal Sharp Wave-Ripples. *Neuron* 100, 1224–1240.e13. [PubMed: 30482688]
- Ryan SJ, Ehrlich DE, Jasnow AM, Daftary S, Madsen TE, and Rainnie DG (2012). Spike-timing precision and neuronal synchrony are enhanced by an interaction between synaptic inhibition and membrane oscillations in the amygdala. *PLoS One* 7, e35320. [PubMed: 22563382]
- Sah P, Faber ES, Lopez De Armentia M, and Power J (2003). The amygdaloid complex: anatomy and physiology. *Physiol. Rev* 83, 803–834. [PubMed: 12843409]
- Schlingloff D, Káli S, Freund TF, Hájos N, and Gulyás AI (2014). Mechanisms of sharp wave initiation and ripple generation. *J. Neurosci* 34, 11385–11398. [PubMed: 25143618]
- Schomburg EW, Anastassiou CA, Buzsáki G, and Koch C (2012). The spiking component of oscillatory extracellular potentials in the rat hippocampus. *J. Neurosci* 32, 11798–11811. [PubMed: 22915121]
- Somogyi P, Freund TF, and Cowey A (1982). The axo-axonic interneuron in the cerebral cortex of the rat, cat and monkey. *Neuroscience* 7, 2577–2607. [PubMed: 7155343]
- Spampanato J, Polepalli J, and Sah P (2011). Interneurons in the basolateral amygdala. *Neuropharmacology* 60, 765–773. [PubMed: 21093462]
- Spampanato J, Sullivan RK, Perumal MB, and Sah P (2016). Development and physiology of GABAergic feedback excitation in parvalbumin expressing interneurons of the mouse basolateral amygdala. *Physiol. Rep* 4, e12664. [PubMed: 26733246]
- Stark E, Roux L, Eichler R, Senzai Y, Royer S, and Buzsáki G (2014). Pyramidal cell-interneuron interactions underlie hippocampal ripple oscillations. *Neuron* 83, 467–480. [PubMed: 25033186]
- Szabadics J, Varga C, Molnár G, Oláh S, Barzó P, and Tamás G (2006). Excitatory effect of GABAergic axo-axonic cells in cortical microcircuits. *Science* 311, 233–235. [PubMed: 16410524]
- Taniguchi H, Lu J, and Huang ZJ (2013). The spatial and temporal origin of chandelier cells in mouse neocortex. *Science* 339, 70–74. [PubMed: 23180771]

- Traub RD, Buhl EH, Gloveli T, and Whittington MA (2003). Fast rhythmic bursting can be induced in layer 2/3 cortical neurons by enhancing persistent Na<sup>+</sup> conductance or by blocking BK channels. *J. Neurophysiol* 89, 909–921. [PubMed: 12574468]
- Varga C, Oijala M, Lish J, Szabo GG, Bezaire M, Marchionni I, Golshani P, and Soltesz I (2014). Functional fission of parvalbumin interneuron classes during fast network events. *eLife* 3, e04006.
- Veres JM, Nagy GA, Vereczki VK, Andrási T, and Hájos N (2014). Strategically positioned inhibitory synapses of axo-axonic cells potentially control principal neuron spiking in the basolateral amygdala. *J. Neurosci* 34, 16194–16206. [PubMed: 25471561]
- Viney TJ, Lasztocki B, Katona L, Crump MG, Tukker JJ, Klausberger T, and Somogyi P (2013). Network state-dependent inhibition of identified hippocampal CA3 axo-axonic cells in vivo. *Nat. Neurosci* 16, 1802–1811. [PubMed: 24141313]
- Washburn MS, and Moises HC (1992). Electrophysiological and morphological properties of rat basolateral amygdaloid neurons in vitro. *J. Neurosci* 12, 4066–4079. [PubMed: 1403101]
- Woodruff AR, and Sah P (2007). Networks of parvalbumin-positive interneurons in the basolateral amygdala. *J. Neurosci* 27, 553–563. [PubMed: 17234587]
- Woodruff AR, Monyer H, and Sah P (2006). GABAergic excitation in the basolateral amygdala. *J. Neurosci* 26, 11881–11887. [PubMed: 17108161]
- Woodruff AR, Anderson SA, and Yuste R (2010). The enigmatic function of chandelier cells. *Front. Neurosci* 4, 201. [PubMed: 21151823]

### Highlights

- Local basolateral amygdala (BLA) circuits generate sharp-wave ripples (SWs) *ex vivo*
- SWs occur with simultaneous synaptic burst inputs in BLA neurons
- A chandelier interneuron discharge can initiate SW bursts through local circuits.
- *In silico* chandelier-interneuron-driven modular microcircuits reproduce SW bursts

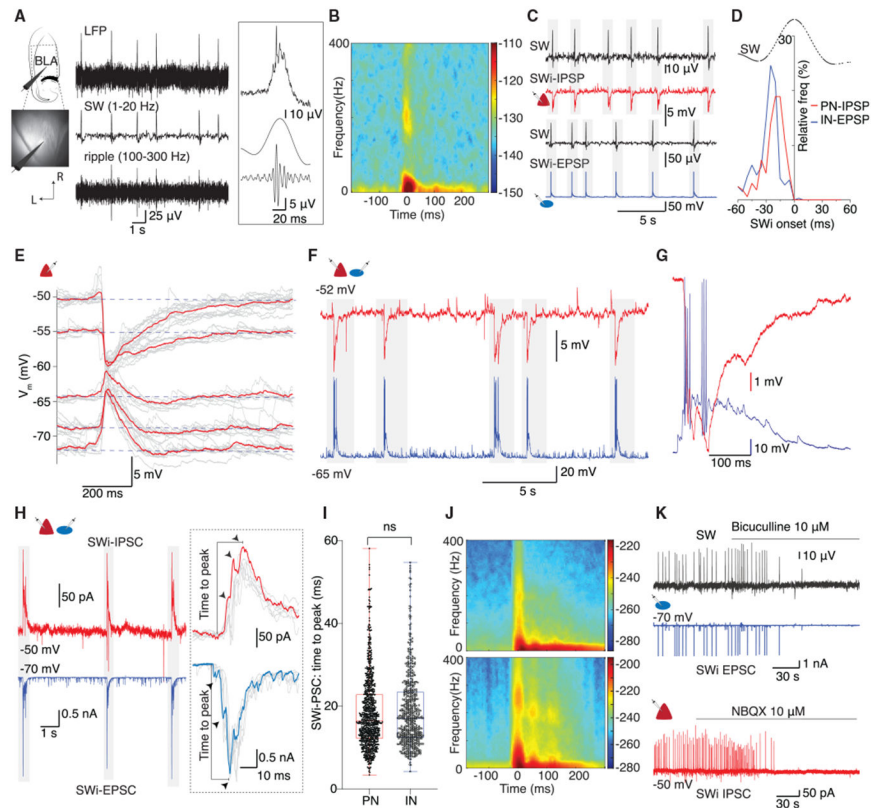


**Figure 1. Sharp-wave ripples in the basolateral amygdala**

(A) Schematic shows the location of the basolateral amygdala (BLA) in an oblique-horizontal brain slice and placement of the recording electrode. The photograph below shows electrode placement to record the local field potential (LFP) in the BLA. L and R mark lateral and rostral directions. Traces on the right show the LFP recorded in wide band (0.1–1 kHz, top), following low pass (1–20 Hz) and high band pass (100–300 Hz) filtering. Inset shows averaged SW in the three frequency domains at a higher temporal resolution showing sharp wave envelope (middle) and occasionally coupled ripples (bottom).

(B) Power spectrum of wideband SWs aligned to the peak, demonstrating enhanced power in the SW (~20 Hz) and ripple frequency (~200 Hz) bands.

(C) Simultaneous LFP and whole-cell recording from a principal neuron (PN, red, top two traces) and interneuron (IN, blue, bottom two traces) for SW-associated intracellular events (SWi). In PNs, SWs were correlated with inhibitory postsynaptic potentials (SWi IPSPs). In INs, SWs were correlated with excitatory post-synaptic potentials (SWi EPSPs) that evoked action potentials (APs).

(D) Distribution of SWi onset in PNs (n = 8, 201 episodes) and INs (n = 12, 345 episodes) with respect to the SW-LFP peak.

(E and F) SWi-IPSP in PNs occur with SWi-EPSPs containing AP burst in INs. (E) Current-clamp recording for SWi from a PN at the indicated membrane potential. Each episode is aligned at the peak of the SWi showing reversal of polarity near –60 mV. (F) Simultaneous whole-cell recordings of a PN (red) and an IN (blue). SW-associated IPSPs in the PN occur time locked with bursts of APs in the IN.

(G) Expanded and overlaid trace of a SW-IPSP in the PN (red) and concurrent SW burst discharges in the IN (blue) shown in (F).

(H–J) SW-associated postsynaptic currents (PSCs) had stereotypical waveform and temporal structure. (H) Voltage-clamp recording from the same cell pair as shown in (F) at the indicated holding potentials illustrating summing inhibitory postsynaptic currents (SWi-IPSCs) in the PN (red) and excitatory postsynaptic currents (SWi-EPSCs) in the IN (blue). Inset, superimposed traces (gray) show stereotypical waveforms of summing postsynaptic currents in the PN and the IN; a single episode highlighted in color shows recurrent (arrow heads) synaptic currents summing to a peak. (I) Times to peak of SW-associated synaptic burst in PNs ( $n = 1,073$  episodes,  $19 \pm 9$  ms) and INs ( $n = 688$  episodes,  $20 \pm 10$  ms) were comparable (Kolmogorov-Smirnov [KS] test,  $p = 0.06$ ). (J) Spectrogram of SWi-IPSCs and SWi-EPSCs shows enhanced power in similar frequency components.

(K) SWs and associated synaptic events blocked by GABA<sub>A</sub> (bicuculline) and AMPA receptor antagonists (NBQX). Top two traces show simultaneously recorded SW (black) and SWi-EPSCs in an IN (blue) abolished by bicuculline. Bottom trace shows SWi-IPSCs in a voltage-clamped PN abolished by NBQX.

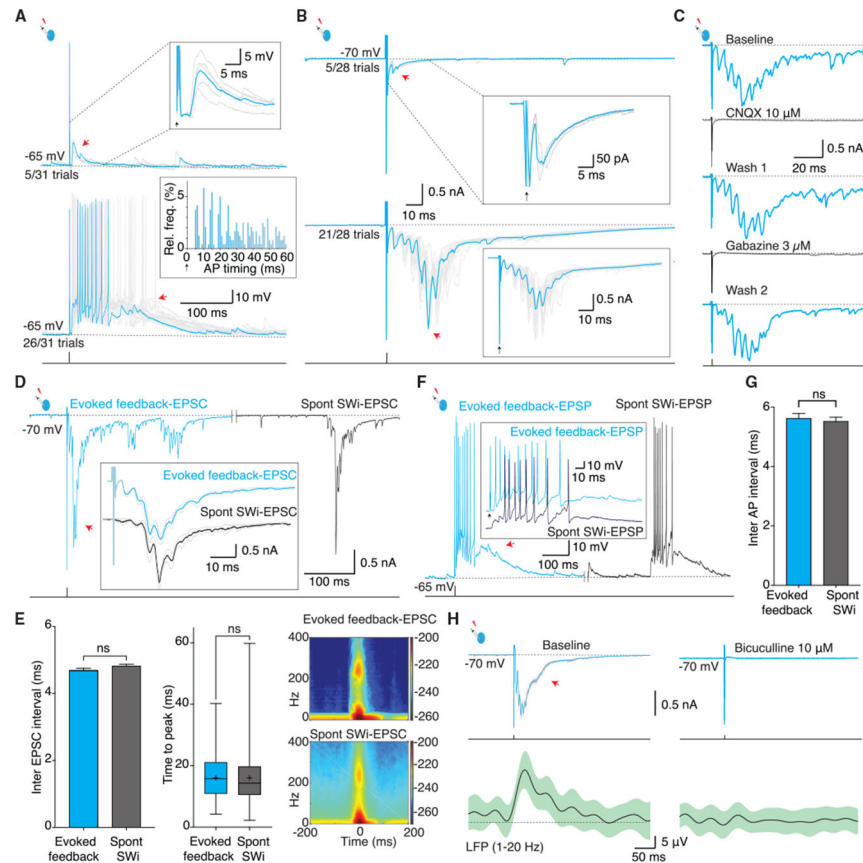


**Figure 2. INs with feedback excitation initiate sharp waves**

(A and B) An AP in putative chandelier INs (ChNs) evoked time-locked multi-synaptic feedback burst. (A) Whole-cell recording from a fast-spiking IN. An AP evoked with depolarizing current injection (1.5 nA, 1 ms, bottom trace) sometimes (5/31) generated a time-locked disynaptic feedback EPSP (red arrow; top traces,  $n = 102$ ); inset shows mean trace of feedback EPSPs (cyan) overlaid on individual trials. Middle traces show trials when the AP evoked a summing EPSP burst, driving time-locked APs ( $n = 19/102$  cells); a single trial highlighted in cyan is overlaid on individual trials. Inset, histogram of APs following the current injection showing time-locked discharge. (B) Voltage-clamp recording (Vh  $-70$  mV) in an IN with feedback excitation. A depolarizing voltage step ( $70$  mV,  $0.5$  ms) evokes an unclamped “action current” followed by a time-locked feedback EPSC (red arrow) in some trials (top traces) or a burst of summing feedback EPSCs (bottom trace). A single episode (cyan) is overlaid on individual trials. Insets show the mean trace in cyan overlaid with individual trials. Note the regular and precise timing of feedback EPSCs. (C) The evoked feedback burst is reversibly blocked by an AMPA receptor antagonist, CNQX (top), and a GABA<sub>A</sub> receptor antagonist, gabazine (bottom). (D–G) Evoked feedback bursts are similar to SW-associated intracellular events (SWi). (D) Voltage-clamp recording showing an evoked feedback EPSC burst in an IN (cyan), and spontaneous SWi in the same cell (black). Inset: enlarged mean ( $\pm 2$  SEM) traces of the evoked feedback EPSC burst (top trace) and spontaneous SWi EPSC in the same cell.

(E) Left and middle, histograms show the IN-evoked feedback burst (468 trials), and spontaneous SWi (712 episodes) have recurring EPSCs at similar time intervals (mean  $\pm$  SEM,  $4.7 \pm 0.06$  versus  $4.8 \pm 0.05$ , Mann-Whitney comparison of ranks,  $p = 0.9$ ) and similar time to peak of the burst (mean  $\pm$  SD,  $16 \pm 7$  ms versus  $16 \pm 8$  ms, Mann-Whitney comparison of ranks,  $p = 0.2$ ). Right, spectrogram of evoked feedback EPSC bursts (top) and SW-associated EPSCs (SWi) in these INs (bottom) show enhanced power in same frequency bands.

(F) Current-clamp recording from an IN with feedback burst. A brief (1.5 nA, 1 ms, bottom trace) current injection evoked an AP followed by feedback EPSPs with an AP burst discharge (cyan); the black trace shows spontaneous SWi EPSP with AP burst discharge in the same cell. Inset, expanded traces of burst discharge in evoked feedback EPSP and SWi EPSP show similar time-locked APs.

(G) Bar graph shows that inter-AP intervals during evoked feedback bursts (blue, 905 trials), and SWi (black, 2,682 episodes) had similar time intervals (mean  $\pm$  SEM,  $5.6 \pm 0.2$  ms versus  $5.5 \pm 0.1$  ms, KS test,  $p = 0.7$ ).

(H) Voltage-clamp recording from an IN (top traces) and simultaneous LFP recording (bottom traces). Left, a brief voltage step (70 mV, 0.5 ms) in the IN evoked a feedback burst and a SW in the LFP (mean  $\pm$  2 SEM), and both events were blocked by bicuculline (right).

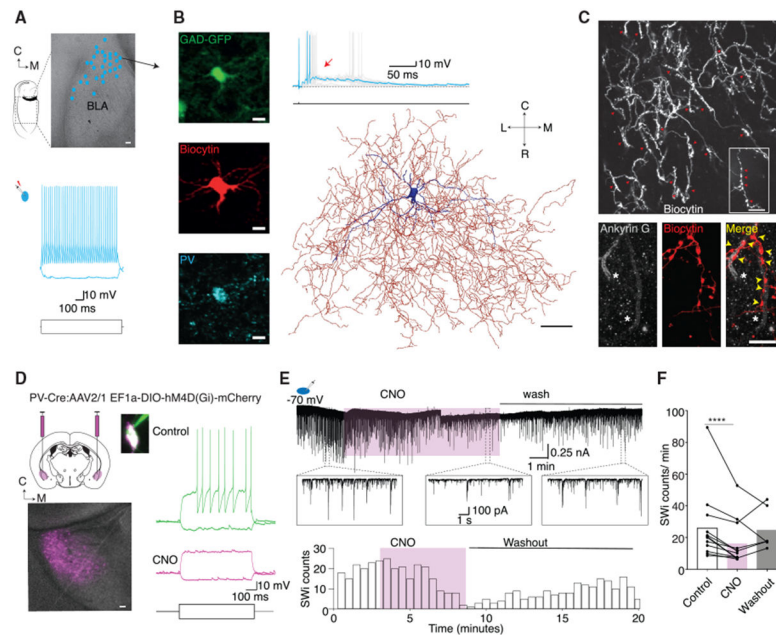


### Figure 3. Chandelier interneuron initiates sharp waves

(A) Image showing the location of recovered INs (cyan dots,  $n = 31$ ) that evoked feedback excitation in the BLA. Scale bar:  $100\ \mu\text{m}$ . Bottom trace shows typical discharge pattern of these INs showing fast-spiking phenotype.

(B) INs with feedback excitation expressed parvalbumin (PV) and showed extensive axonal innervation in the BLA. Top panel shows whole-cell recording from an IN in a GAD-67 EGFP mouse marked by an arrow in (A) in which a brief current injection to drive an AP evoked a feedback EPSP with a burst of APs (right). Left middle and bottom panels show the same cell recovered with biocytin (red) and positive for PV (bottom). Scale bar:  $10\ \mu\text{m}$ . Right panel shows digital reconstruction of the same IN with the soma and dendrite in blue and axon in red. Scale bar:  $50\ \mu\text{m}$ .

(C) The axonal plexus of INs with feedback contained strings of synaptic bouton “cartridges” in close approximation to the axon initial segment marker Ankyrin G. Top panel,  $20\times$  magnified image of recovered axonal plexus from an IN with feedback burst showing multiple strings of synaptic bouton cartridges (red arrows); the inset shows a  $100\times$  magnification of a cartridge containing a string of synaptic boutons (red arrows). Bottom panels from the same axon at  $100\times$  magnification and panels from left to right show two axon initial segments stained for Ankyrin G (white), biocytin-recovered cartridge synaptic boutons in the same location, and superimposed images of biocytin and Ankyrin G staining exhibits close approximation of cartridge synaptic boutons (red) on Ankyrin G (white). Scale bar:  $10\ \mu\text{m}$ .

(D–F) Chemogenetic silencing of PV-INs reduces sharp waves. (D) Schematic illustrates delivery of the double-floxed inhibitory DREADD hMDGi into the BLA in PV-Cre mice. Bottom image shows horizontal brain slice with PV-INs in the BLA region expressing hMDGi (magenta). Caudal and medial directions indicated as C and M. Scale bar:  $100\ \mu\text{m}$ . Image on the right shows the soma of a PV-IN expressing mCherry (magenta) filled with Alexa 488 (green) from the recording patch pipette. Current-clamp traces show the

typical fast-spiking phenotype evoked with depolarizing current step, which was blocked after exposure to CNO 15  $\mu$ M.

(E) Current trace from voltage-clamp recording in an IN showing spontaneous SWi EPSCs. The plot below shows the SWi EPSC incidence in the same IN. Application of CNO (15  $\mu$ M, magenta) reduced the SWi incidence. Insert, enlarged traces of SWi EPSCs reduced by silencing of PV-INs. (F) Graph shows the effect of CNO on SWi incidence recorded in slices expressing hMDGi receptors (SW-EPSCs, n = 7 cells/slices; SWi-IPSCs, n = 7 cells/slices, Wilcoxon rank-sum test,  $p < 0.0001$ ).

Author Manuscript

Author Manuscript

Author Manuscript

Author Manuscript

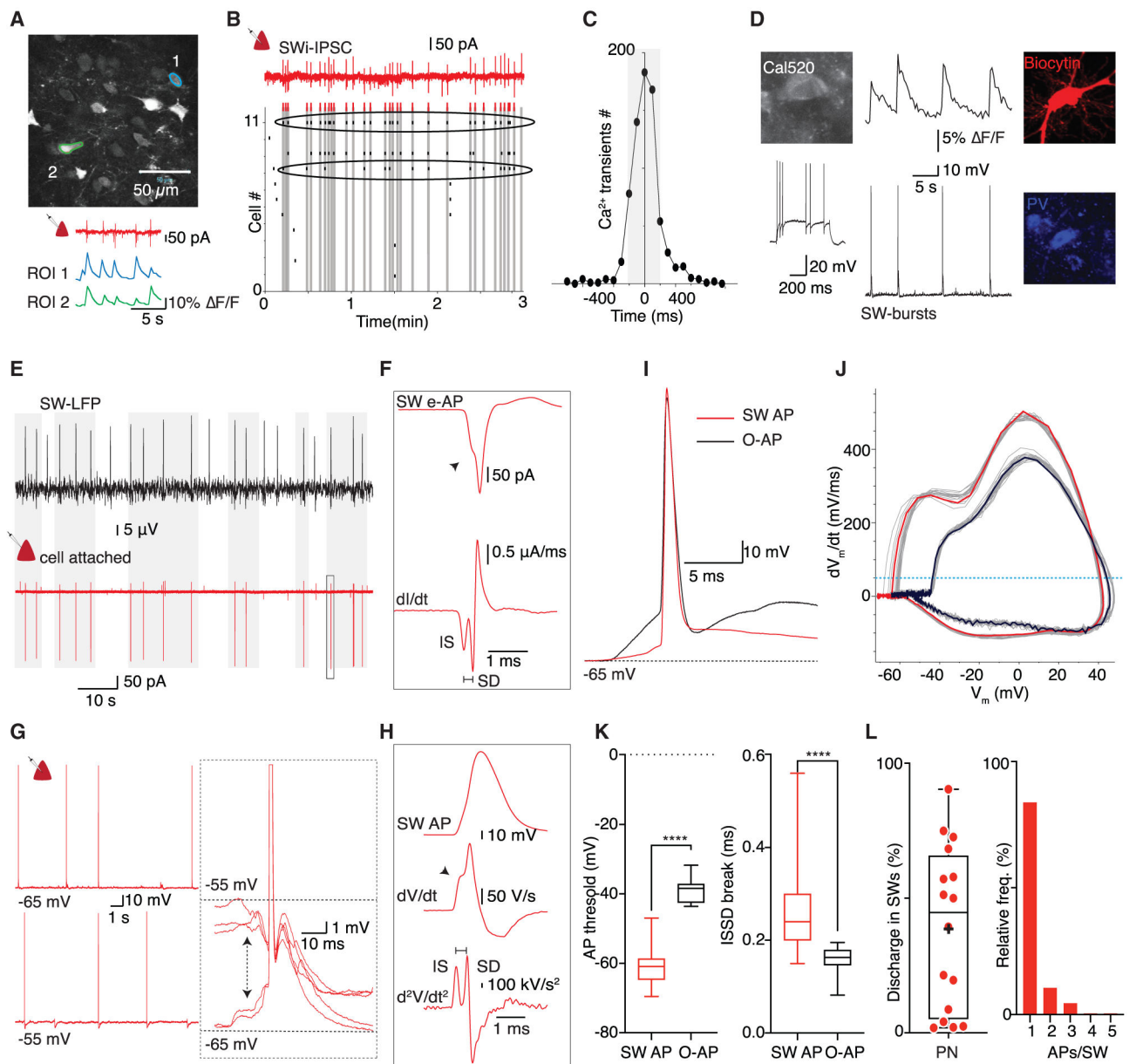


**Figure 4. Principal neurons discharge sparsely during sharp waves with antidromically initiated APs**

(A) Population activity in the BLA imaged using the fluorescent calcium indicator Cal-520. Image shows neurons loaded with Cal-520, with two selected neurons (region of interest [ROI]) marked (1 and 2). Bottom traces show SWi IPSCs from a PN, and simultaneously captured calcium transients (CaTs;  $F/F\%$ ) from cells 1 and 2.

(B) Population activity during SWi. Top trace (red) shows SWi-IPSCs recorded from a voltage-clamped PN. Raster plot shows calcium transients from 11 active cells during the imaging time window. Gray bars mark CaTs that occurred concurrently with SWs. CaTs from two highlighted cells illustrate consistent (top) and sparse (bottom) engagement during SWs.

- (C) Distribution shows timing of CaTs aligned to the SWi peak. Most (86%) CaTs occurred within  $\pm 200$  ms (gray highlight) of a SWi ( $n = 8$  slices, 726 episodes).
- (D) Cells with consistent CaTs time locked with SWi are INs ( $n = 4$ ). Left, image shows whole-cell recording in a Cal520-loaded neuron; current injection evoked AP discharge in the same cell. Middle, top trace shows spontaneous CaTs (top) in the cell and report APs during the SWi (bottom). Right, same cell recovered by staining for biocytin (top), also stained positive for PV (bottom).
- (E) Simultaneous recording of LFP (black) showing SWs and cell-attached recording from a PN (red) showing extracellular APs (e-APs) during some (gray bars) but not all SWs.
- (F) Top trace shows a representative SW-associated e-AP (SW e-AP) with inflection (arrow) in the rising phase and its first order time derivative ( $dI/dt$ , bottom trace) showing two peaks corresponding to the initial segment (IS) and somato-dendritic (SD) components of the e-AP (Figures S6A-S6C). The latency between the IS and SD (IS-SD break) is marked.
- (G) Following conversion to whole-cell configuration, some PNs continued to discharge during SWi-IPSPs ( $n = 10$ ). Top trace: representative intracellular AP from resting membrane potential. Bottom trace: same cell at  $-50$  mV showing the AP discharge within SWi-IPSP. Inset: superimposed SWi in the PN recorded from rest ( $-65$  mV) and following depolarization ( $-55$  mV). AP discharge is preceded by IPSPs (bidirectional arrow).
- (H) Representative intracellular SW-AP (top trace) and first order time derivative ( $dV/dt$ , middle trace) and the second order time derivative ( $d^2V/dt^2$ , bottom trace) showing two peaks corresponding to IS and SD components; arrow marks the transition from the IS to the SD component (Figure S6D).
- (I) Superimposed traces show an intracellular AP recorded from a PN in SWi (SW-AP, red) and an orthodromic AP evoked by glutamatergic EPSP (o-AP; black). Note that the SW-AP rises abruptly from a more negative membrane potential compared to that of the evoked o-AP.
- (J) Phase plots of SW-APs (single AP highlighted in red) and o-APs (single trace highlighted in black). The AP threshold, defined as the membrane potential ( $V_m$ ) when  $dV/dt = 50$  mV/ms, is indicated by the horizontal dotted line. AP threshold for SW-APs is more negative than o-APs.
- (K) Comparison of spike threshold and IS-SD break in SW-APs and o-APs. Left panel plots the difference in AP threshold (SW-AP,  $-61 \pm 4$  mV,  $n = 94$ ; versus o-AP,  $39 \pm 3$  mV,  $n = 197$ , t test,  $p < 0.0001$ ). Right panel shows that the IS-SD break measured in SW-APs (including e-APs recorded in cell attached configuration,  $0.26 \pm 0.07$  ms,  $n = 313$ ; Figures S6A and S6B) was wider than in o-AP ( $0.15 \pm 0.03$  ms, KS test,  $p < 0.0001$ ).
- (L) PNs discharge sparsely in SWs. Left, participation rate of PNs with AP discharge in SWs ( $n = 16$ ); right, number of APs discharged by individual PNs in each SW.

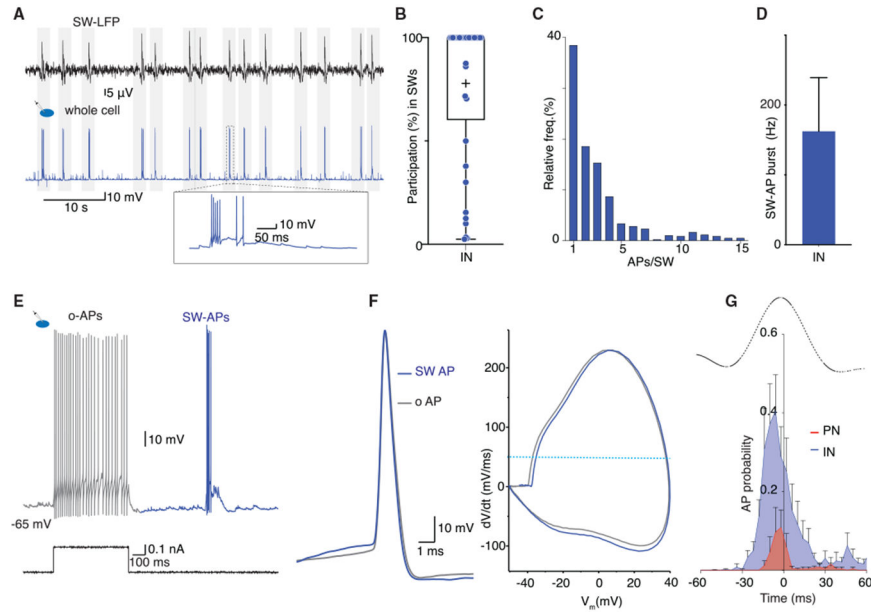


**Figure 5. Interneurons are driven orthodromically and discharge a burst of action potentials during sharp waves**

(A) Simultaneous recording of LFP SWs (top) and whole-cell recording in an IN shows AP discharge with every SW. Inset: expanded trace of a SWi-EPSP with AP burst.

(B) Participation of INs with AP discharge during SWs. Each dot shows participation rate with discharge during the SW from individual INs (n = 37); +, the mean participation rate.

(C) Bar graph plotting the number of APs fired by individual INs in each SW (n = 2,827 episodes).

(D) Burst frequency of IN discharge during SWs (mean ± SD).

(E and F) SW-APs in INs are evoked by orthodromic excitation. (E) Current clamp recording in an IN showing response to depolarizing current injection step evoked o-APs (gray) and a spontaneously occurring SW-AP burst (blue). (F) Left, superimposed traces of the first SW-AP (blue) and the first o-AP (gray) in the same IN illustrating similar waveforms. Right, superimposed phase plot of the SW-AP and the o-AP. The horizontal dotted line marks AP threshold, defined as  $dV/dt = 50$  mV/ms.

(G) Distribution shows AP discharge probability for PNs (red, n = 5) and INs (blue, n = 8) with respect to the peak of simultaneously recorded SW (LFP) (black trace). Error bars: SEM. INs discharge early in the rising phase and continue throughout the SW. PNs are engaged sparsely and mostly do not discharge after the SW peak.

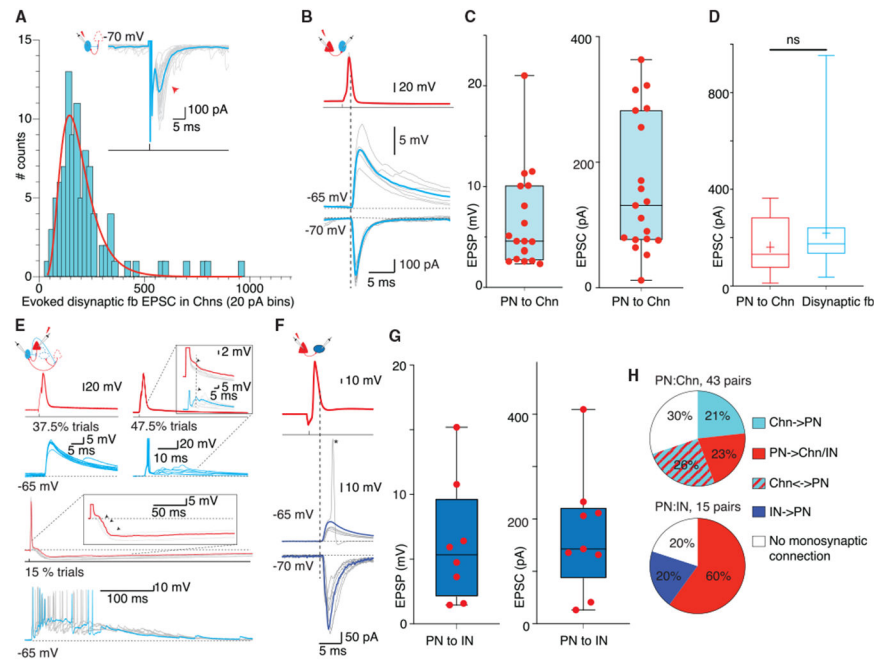


**Figure 6. Local glutamatergic connections drive feedforward INs in sharp-wave bursts**

(A) Schematic of Chn disynaptic feedback circuit and trace show voltage-clamp recording from a representative Chn. A brief voltage step (70 mV, 0.5 ms) evoked a feedback EPSC (mean in cyan overlaid on individual trials). Histogram shows distribution of mean amplitude of disynaptic feedback EPSCs ( $n = 96$ ) fitted with a logarithmic curve (red).

(B) Paired recording from a PN (red) and a Chn (blue). Top, superimposed traces show an AP evoked by current injection (2.5 nA, 1 ms) in the PN evoked a monosynaptic EPSP (current clamp, middle) and large EPSCs (voltage clamp, bottom trace) in the Chn; mean trace in color overlaid on individual trials. The dotted line marks the peak of the AP.

(C) Panels show amplitude of a pre-PN AP evoked monosynaptic EPSPs and EPSCs in Chns. Each dot represents the mean amplitude recorded in individual pairs.

(D) PN-evoked monosynaptic EPSCs in Chn re comparable to the evoked disynaptic feedback EPSC. Comparison of evoked monosynaptic EPSCs ( $n = 19$ ,  $161 \pm 108$  pA) and di-naptic feedback EPSCs in Chns ( $n = 96$ ,  $218 \pm 158$  pA, KS test,  $p = 0.07$ ).

(E) Feedforward circuits between PNs and Chns. Paired recording from a PN (red) and Chn (blue). Top left, current injection (2.5 nA for 1 ms) evoked an AP in the PN and monosynaptic EPSP in the Chn (bottom, cyan). Top right, traces from the same pair showing trials when the PN input triggered discharge in the Chn that was followed by feedback EPSP. Inset shows enlarged traces from the PN and Chn, with feedforward IPSP (arrow) in the PN, simultaneously with feedback EPSP in the Chn (dotted line). Bottom, traces from the same pair on a compressed timescale showing trials when the PN input triggered an AP in the Chn. The feedback EPSP triggers an AP burst and a summing IPSP in the PN. Individual trials in gray and a single trial highlighted in color. Inset, enlarged traces of the PN membrane potential showing burst of IPSPs (arrow).

(F) PNs provide large inputs to INs without feedback excitation (non-Chn). Paired recording of PN (red) and non-Chn (blue). Current injection (2.5 nA for 1 ms) in the PN evoked an AP and monosynaptic EPSP (middle, current clamp) or EPSC (bottom, current clamp) in the

IN. In some trials, the PN input evoked an AP in the IN (17% of trials). Note the lack of feedback EPSP in this IN.

(G) Mean amplitude of evoked EPSPs and EPSCs in non-Chns. Each dot represents the mean amplitude from individual pairs.

(H) Pie charts show proportions of synaptic connectivity between PN-Chn (top) and PN-IN pairs (bottom).

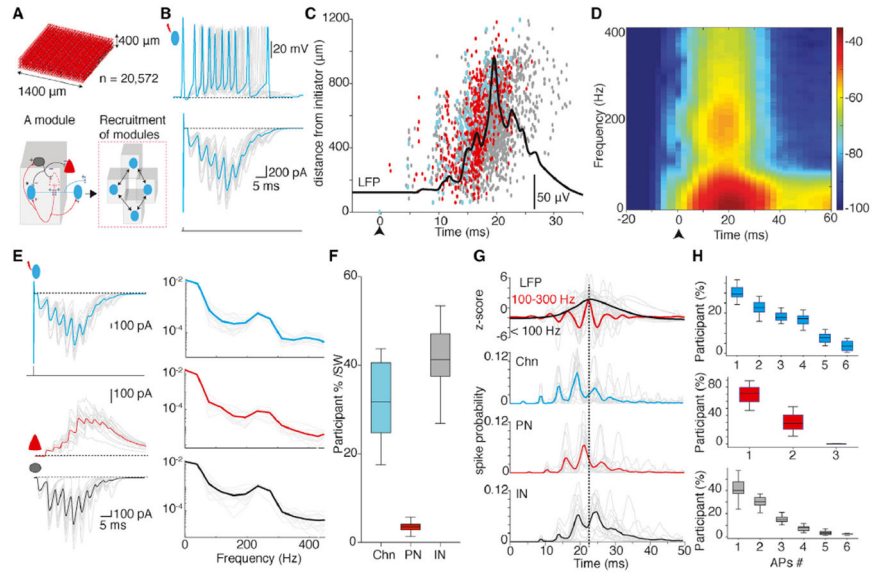


**Figure 7. A network model with Chn-driven circuit modules reproduces sharp waves**  
 (A) Top, network model constructed with 20,572 neurons occupying a volume of  $1,400 \times 1,400 \times 400 \mu\text{m}$  comprising the following three cell types (proportions): PNs (80%), basket INs (18%), and Chns (2%). Bottom, schematic of circuit organization in a single module consisting of a Chn (cyan) connected to a PN (s) (red) that then projects to an IN (s) (gray) and other Chn (s); +/- indicate excitatory/inhibitory connection. Adjacent modules recruited through Chns.

(B) A single AP discharge in a Chn in the network model evoked a time-locked feedback burst. Gray traces are from individual Chns ( $n = 16$ ) overlaid with the mean (cyan). Top, current-clamp traces show that a single AP in a Chn-evoked feedback EPSP that triggered time-locked burst of APs; bottom, voltage-clamp traces show a single AP (unclamped action current) in a Chn followed by time-locked burst of feedback EPSCs.

(C) A Chn-evoked feedback burst occurred with a population burst and transition in the LFP in the network model. Raster plot shows the timing of spike discharge of Chns (cyan), PNs (red), and INs (gray) during a Chn (cyan)-evoked population burst against distance from the initiator (upward arrow at time zero). The wide-band LFP at the center of the model during the population burst is overlaid in black. Note that the initiating Chn (at time zero) drives only two PNs (red) before the activity propagates through the network.

(D) Spectral analysis of the LFP at the center of the network model from 16 trials of evoked population burst from different Chns shows enhanced power in the SW and ripple frequency bands.

(E) Chns in the model initiated an IPSC burst in PNs and an EPSC burst in INs with intrinsic frequency of  $\sim 250$  Hz. Left, top to bottom traces show a superimposed feedback EPSC burst (gray) from 16 Chns overlaid with mean (cyan); simultaneously recorded synaptic currents in PNs (middle) show a burst of IPSCs (gray, mean in red) and in INs (bottom) show a burst of EPSCs (gray, mean in red). Right, (top to bottom) spectral analysis of synaptic current bursts in Chns, PNs, and INs shows enhanced power at  $\sim 250$  Hz. Mean highlighted and overlaid on individual episodes (gray).

(F) Proportion of cells recruited by the initiating Chn to discharge AP(s) in each cycle.

(G) Top traces show the LFP from 16 trials with each trial initiated by different Chns and band-pass filtered for SW (black) and ripples (red). Bottom plots show the spike probability of Chns, PNs, and INs during SWs. Individual trials in gray and mean overlaid in color. The vertical dotted line marks the peak of the SW.

(H) Cell-type-specific AP discharge during a Chn evoked a SW in the network model (n = 16 trials). Note Chns and INs burst fire multiple APs, whereas PNs predominantly discharge a single AP.

## KEY RESOURCES TABLE

REAGENT or RESOURCE	SOURCE	IDENTIFIER
Antibodies		
Rabbit anti-Ankyrin G	Santa Cruz	Cat#: sc28561; RRID:AB_633909
Mouse anti-parvalbumin	Sigma-Aldrich	Cat#: P3088; RRID:AB_477329
Goat anti-mouse, Alexa 405	Life Technologies	Cat#:A31553;RRID:AB_221604
Goat anti-rabbit, Alexa 647	Invitrogen	Cat#:A21245;RRID:AB_2535813
Alexa 555-Streptavidin	Invitrogen	Cat# S32355;RRID:AB_2571525
Alexa 647-Streptavidin	Invitrogen	Cat#: S21374;RRID:AB_2336066
Bacterial and virus strains		
pAAV-EF1a-DIO-hM4D(Gi)-mCherry	Addgene	Plasmid#: 50461;RRID:Addgene_50461
Chemicals, peptides, and recombinant proteins		
Cal520 AM	Abcam	CAT#: 21130
Bicuculline	Tocris	CAS# 485-49-4
Picrotoxin	Sigma-Aldrich	CAS#: 124-87-8
Gabazine	Tocris	CAS#: 104104-50-9
NBQX	Tocris	CAS# 118876-58-7
CNQX	Tocris	CAS#: 115066-14-3
Clozapine-N-oxide	AK Scientific	CAS#: 34233-69-7
Biocytin	Sigma-Aldrich	CAS#: 576-19-2
Linopiridine	Tocris	CAS#: 113168-57-3
Experimental models: organisms/strains		
Rat: Sprague Dawley	Animal facility, Queensland Brain Institute, The University of Queensland	
Rat: Wistar	Animal facility, Queensland Brain Institute, The University of Queensland	
Mice: C57BL/6NCrj xCBA/JNCrj) F1	Animal facility, Queensland Brain Institute, The University of Queensland	
Mice: B6;129P2-Pvalb <sup>tm1(cre)Arbr/J</sup>	Animal facility, Queensland Brain Institute, The University of Queensland	
Mice: WT (C57BL/6 and BALB/c background)	Animal facility, Queensland Brain Institute, The University of Queensland	
Software and algorithms		
Axograph X	Axograph Scientific	RRID:SCR_014284
NeuroLucida	MicroBrightField	RRID: SCR_001775
NEURON	<a href="https://neuron.yale.edu/neuron/">https://neuron.yale.edu/neuron/</a>	RRID: SCR_005393
MATLAB (R_2018a)	Mathworks	RRID: SCR_001622
Fiji(ImageJ)	<a href="https://imagej.nih.gov/ij/">https://imagej.nih.gov/ij/</a>	RRID: SCR_002285
GraphPad Prism (Version 7 and 8)	GraphPad	RRID: SCR_002798
Other		
Vibrotome	Leica	VT1000S
Patch clamp amplifier	Molecular Devices	Multiclamp 700A and 700B
ITC-16 A/D converter	InstruTECH	

REAGENT or RESOURCE	SOURCE	IDENTIFIER
HumBug	Digitimer	

Author Manuscript

Author Manuscript

Author Manuscript

Author Manuscript